



저작자표시-비영리-변경금지 2.0 대한민국

이용자는 아래의 조건을 따르는 경우에 한하여 자유롭게

- 이 저작물을 복제, 배포, 전송, 전시, 공연 및 방송할 수 있습니다.

다음과 같은 조건을 따라야 합니다:



저작자표시. 귀하는 원저작자를 표시하여야 합니다.



비영리. 귀하는 이 저작물을 영리 목적으로 이용할 수 없습니다.



변경금지. 귀하는 이 저작물을 개작, 변형 또는 가공할 수 없습니다.

- 귀하는, 이 저작물의 재이용이나 배포의 경우, 이 저작물에 적용된 이용허락조건을 명확하게 나타내어야 합니다.
- 저작권자로부터 별도의 허가를 받으면 이러한 조건들은 적용되지 않습니다.

저작권법에 따른 이용자의 권리는 위의 내용에 의하여 영향을 받지 않습니다.

이것은 [이용허락규약\(Legal Code\)](#)을 이해하기 쉽게 요약한 것입니다.

[Disclaimer](#)

Doctor of Philosophy

Research on statistical model based surgical planning
and advanced registration methods for image-guided
surgery

The Graduate School
of the University of Ulsan

Department of
Electrical, Electronic,
and Computer
Engineering

Hang Phuong Nguyen

Research on statistical model based surgical planning
and advanced registration methods for image-guided
surgery

Supervisor: Professor Sungmin Kim

A Dissertation

Submitted to

the Graduate School of the University of Ulsan

In partial Fulfillment of the Requirements

for the Degree of

Doctor of Philosophy

by

Hang Phuong Nguyen

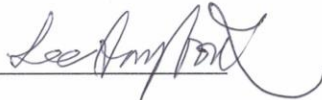
Department of Electrical, Electronic and Computer Engineering

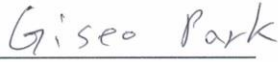
University of Ulsan, Korea

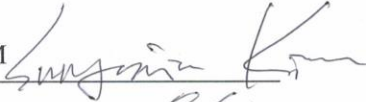
August 2024


Research on statistical model based surgical planning and advanced registration methods for image-guided surgery


This certifies that the dissertation thesis of
Hang Phuong Nguyen is approved.

Committee Chair: Professor SANG-WOOK LEE 

Committee Member: Professor GISEO PARK 

Committee Member: Professor SUNGMIN KIM 

Committee Member: Professor UICHEUL YOON 

Committee Member: Professor JEONGHUN KU 

Department of Electrical, Electronic and Computer Engineering
University of Ulsan, Korea
August 2024

Abstract

Image-guided surgery (IGS), which modernizes surgery and makes it safer and less invasive, has been receiving a lot of interest in recent years. In the preoperative context, diagnostic imaging, such as computer tomography (CT) and magnetic resonance imaging (MRI) provides a foundation for surgical planning including the delineation of surgery target, the surrounding anatomies, and the surgical strategy or trajectory to the target. Additionally, using a statistical atlas in the preoperative stage provides a comprehensive anatomical reference that helps surgeons to better understand complex anatomical variations in a large dataset and spatial relationships between involving individuals, therefore allowing for automatic personalized surgical planning. Such preoperative images and surgical planning information are registered to intraoperative coordinates using a navigation system such as Optical Tracking System (OTS) to visualize tracked instruments in relation to preoperative images.

This dissertation seeks to solve three interesting research questions in the preoperative and intraoperative process. The dissertation includes work encompassing: (1) proposing a framework for multimodal image registration between CT and MRI; (2) proposing a computer-assisted surgical planning method using statistical atlas and applying to the humerus surgery scenario; and (3) proposing a dynamic touchable region model applied to a framework for markerless registration in the intraoperative stage.

Acknowledgement

First and foremost, it is with great sincerity that I wish to extend my profound appreciation and thankfulness to my advisor, Professor Sungmin Kim, who has provided support and encouragement for my research in the Image Guided Surgery and Robotic Laboratory (IGSR). The mentorship, motivation, and dedication to science by him have profoundly impacted my wonderful Ph.D journey. He has taught me much about scientific communication, which is shown in this dissertation in every aspect. His warmth and patience have helped me keep going and make improvements myself during this journey. I am deeply grateful as a student under his guidance.

I would like to express my gratitude to all IGSR lab members, I could not have completed my dissertation without your support and encouragement. I would especially like to thank Taeho Kim, who and I are one of first our Professor's students, for his generous advice and assistance with everything in work and life.

I feel extremely lucky to have loving family and friends who have helped me through everything. I would especially like to thank my friends Thanh Hai Phan, Quy Lam Hoang and his family Hong Van Bach and an adorable baby Min, Huu Lam Phan and his family Thi Quy Nguyen and a cute boy Binh, Thi Huong Le, Thi Trang Le, Chanh Trung Nguyen. Through the challenges, many tears, joy, and a lot of laughing, you have been incredibly encouraging and supportive of me with much love.

Finally, to my parents, my sister, and my brother, who love me in every way possible. This journey would not complete without your endless love and support.

Table of Contents

CHAPTER 1. INTRODUCTION	1
1.1. Overview	1
1.1.1. Historical review about Image-guided Surgery	1
1.1.2. Clinical-application areas of Image-guided Surgery	2
1.1.3. Framework of Image-guided surgery.....	5
1.2. Dissertation outline	6
CHAPTER 2. FEATURE-BASED MULTIMODAL IMAGE CT-MRI REGISTRATION ASSISTED BY SEGMENTATION	7
2.1. Introduction	7
2.1.1. Related work	7
2.1.2. Contribution	11
2.2. Materials and Methods	11
2.3. Results	15
2.3.1. Segmentation results	15
2.3.2. Registration results.....	17
2.4. Discussion and Conclusion	18
CHAPTER 3. FEASIBILITY STUDY FOR THE AUTOMATIC SURGICAL PLANNING METHOD BASED ON STATISTICAL MODEL	20
3.1. Introduction	20
3.1.1. Related work	20
3.1.2. Contribution and acknowledgement	21
3.2. Materials and Methods	22
3.2.1. Preprocessing and data splitting.....	22
3.2.2. Building average population model	23
3.2.3. Evaluation before surgical planning	24
3.2.4. Validation for surgical planning.....	24
3.3. Results	25
3.4. Discussion and Conclusion	28
CHAPTER 4. MARKERLESS REGISTRATION APPROACH USING DYNAMIC TOUCHABLE REGION MODEL	30
4.1. Introduction	30
4.1.1. Related work	30
4.1.2. Contribution and acknowledgment	31

4.2. Materials and Methods	32
4.2.1. Definition of the Dynamic Touchable Region	32
4.2.2. Registration using Dynamic Touchable Region.....	34
4.2.3. Data analysis	35
4.3. Experiment	35
4.4. Results	39
4.4.1. Evaluation of DTR.....	39
4.4.2. ICDTP registration.....	41
4.5. Discussion	45
4.6. Conclusion	47
CHAPTER 5. CONCLUSION	49
REFERENCES	51

List of Tables

Table 2-1: Detailed information of CT and MRI images used for multimodal registration	12
Table 2-2: Statistics about the CT and MRI datasets	13

List of Figures

Figure 1-1: Common applications of IGS [4], [5], [6], [7].	2
Figure 1-2: Image-guided surgery framework.	5
Figure 2-1: The proposed framework of MRI-CT multimodal image registration.....	12
Figure 2-2: Comparison between manually segmentation and nnU-Net-based segmentation at different liver latitudes for different patients. Red mask: liver segmentation predicted by nnU-Net; Blue mask: liver segmentation ground truth.	15
Figure 2-3: Dice similarity coefficients between liver segmentation ground truth and nnU-Net liver segmentation prediction of 13 CT and 15 MRI images.....	16
Figure 2-4: Overlaid registration results with CT (target) and MRI (source). Source: Red color presents liver segmentation prediction using nnU-Net for MRI; Target: Blue color presents CT liver ground truth, Violet color presents overlap between the registered MRI liver mask and the CT ground truth.	17
Figure 2-5: Registration evaluations presented by Dice coefficient and Average Symmetric Surface Distance.....	18
Figure 3-1: Surgical planning framework using the average population model.....	22
Figure 3-2: Eleven clinical landmarks were used for evaluation and validation.	24
Figure 3-3: Distance models and correspondence histograms of distance values for each sub-dataset: A) Female-Left, B) Female-Right, C) Male-Left, D) Male-Right.	25
Figure 3-4: The explained variation of the SSM I each sub-dataset: a) Female-Left, b) Female-Right, c) Male-Left, d) Male-Right.	26
Figure 3-5: Humerus landmarks differences between the ground truth and prediction using SSMs in case of Female subjects: A) Left humerus (p-value < 0.05), B) Right humerus (p-value < 0.05).....	27
Figure 3-6: Humerus landmarks differences between the ground truth and prediction in case of Male subjects: A) Left humerus (p-value < 0.05), B) Right humerus (p-value < 0.05).	28
Figure 4-1: Markerless registration framework based on the ICDTP.	32
Figure 4-2: Procedure for the DTR definition. ISS is noted for Intrinsic Shape Signatures.....	33
Figure 4-3: Change of shape from the original sphere (a) to the DTR (b-d), $\mathbf{0} < \lambda \mathbf{i} \leq \mathbf{1}$	34
Figure 4-4: Geometrical model: a) Designed by 3D CAD software, b) Synthetic CT data simulation, c) Real phantom.....	36

Figure 4-5: Skull phantom: a) 3D model built by laser scan data and a group of fiducials and targets, b) Real phantom and two notches serving as targets.....	36
Figure 4-6: Spine phantom: a) 3D model built by simulated computer tomography data and a group of fiducials and targets, b) Real phantom built by a 3D printer and its holder, c and d) Three notches serving as targets.	37
Figure 4-7: Separable skull phantom: a) 3D model built by real CT data and a group of fiducials, b) Real phantom, c) A group of three deep targets inside the separable skull model, d) Three deep targets inside the real phantom.	38
Figure 4-8: Setup for experiment.....	39
Figure 4-9: Three examples of principal component variation changing the DTR. The blue region presented the original sphere while the red region showed the dynamic touchable region.	40
Figure 4-10: Dynamic touchable region used for markerless registration applied to a) skull model, b) spine model, and c) separable skull model.	41
Figure 4-11: FRE and RRE for the skull phantom in a) single-user study and b) multi-user study.	42
Figure 4-12: FRE and RRE for the spine phantom in a) single-user study and b) multi-user study.	42
Figure 4-13: TREs with skull phantom for: a) single-user study (p-value < 0.05) and b) multi-user study (p-value < 0.05).	43
Figure 4-14: TREs with the spine phantom when tested with three targets in a) Single-user experiment (p-value < 0.001), b) Multi-user experiment (p-value < 0.05).....	44
Figure 4-15: TREs of the separable skull phantom with three deep targets: a) Single-user experiment (p-value < 0.05), b) Multi-user experiment (p-value < 0.05).....	45
Figure 4-16: Comparison of TREs between sphere-only method and DTR-based method applying to the spine model in the single-user experiment (p-value = 0.01).....	46
Figure 4-17: TREs at different radiuses of DTR applying for the spine model in the single-user experiment.	47

Chapter 1. Introduction

1.1. Overview

Image-guided surgery (IGS) is a medical procedure in which real-time images of the inside of the patient are provided by computer-based systems to assist surgeons in precisely interpreting and targeting surgical regions [1]. Significant developments in computer-based processing and medical imaging modalities over the last few decades have facilitated the IGS dramatically. This paragraph provides a brief overview of the historical review, discusses some clinical applications in which IGS plays an important role in enabling procedures and improving accuracy, and describes functional components in a framework of image-guided surgery.

1.1.1. Historical review about Image-guided Surgery

Image-guided surgery (IGS) has emerged as a significant advancement in modern surgery due to its ability to improve surgical precision, efficiency, and safety, particularly in less invasive procedures. The evolution and development of IGS could be divided into five progresses including early development, emergence of stereotactic system, integration of imaging modalities, advancements in navigation technology, and robotics and minimally invasive surgery.

- **Early development (1970s – 1980s):** First, the invention of medical imaging technologies like Computer Tomography (CT) and Magnetic Resonance Imaging (MRI) in the 1970s set the groundwork for the early identification of IGS. These technological advancements made it possible to see inside anatomical regions with great delineation. In order to provide surgeons with intraoperative guidance, researchers have been investigating the integration of different imaging modalities into surgical operations since the 1980s.
- **Emergence of Stereotactic systems (1980s – 1990s):** A major factor in the early development of IGS was stereotactic systems, which pinpoint body structures using three-dimensional coordinates. These devices made it possible to precisely target lesions within the brain or structures during neurosurgical treatments. During surgery, preoperative images were registered with the patient's anatomy using stereotactic frames and fiducial markers [2], [3].
- **Integration of Imaging Modalities (1990s – 2000s):** The 1990s and 2000s noticed the integration of several imaging modalities into IGS systems made easier by developments in computer technology and imaging modalities. Surgeons could combine many medical imaging modalities such as CT, MRI, ultrasound, and other imaging modalities for improved visualization during surgeries. This integration presented more precise navigation and better surgical results in difficult and precision-required procedures such as neurosurgery, orthopedic surgery, and oncology surgery.
- **Advancement in Navigation technology (200s to present):** Significant developments in navigation technology occurred in the 2000s, including the establishment of optical and electromagnetic tracking systems. Comparing these systems to more conventional stereotactic systems, the accuracy and flexibility were

increased. Furthermore, real-time imaging during surgery was made possible with the introduction of intraoperative imaging technologies involving intraoperative CT and MRI.

- **Robotics and minimally invasive surgery (2000s to present):** The possibilities of minimally invasive surgery have been further enhanced by the integration of IGS with robotics. Surgeons can conduct complex procedures with better control and precision using robotic devices that integrate with imaging guidance. These systems provide accurate and dexterous motions within the body. Robotics and image guidance together have revolutionized several fields, including laparoscopic and robot-assisted surgery.

Ongoing research expects that the IGS will likely continue to integrate artificial intelligence and machine learning technologies in the future. The efficiency and accuracy of surgical procedures can be improved by using these technologies to support image registration, surgical planning, and real-time navigation. Furthermore, developments in augmented reality could allow surgeons access to virtual navigation and visualization capabilities directly within the surgical regions.

Finally, from an idea born in the early days of medical imaging, IGS has developed into a highly advanced suite of technologies that are essential to modern surgical procedures and allow for less invasive, safer, and more accurate treatments in a variety of surgical fields.

1.1.2. Clinical-application areas of Image-guided Surgery

Thoracoabdominal interventions, orthopedics, cardiology, and neurosurgery are common main applications of IGS because IGS not only provides real-time visualization of internal organs and surgical instruments, but also allows surgeons to navigate through complex structures of the treatment regions with high precision and reducing the risk of damage to critical areas and improving patient outcomes [1]. Figure 1-1 presents some common applications in the IGS field.

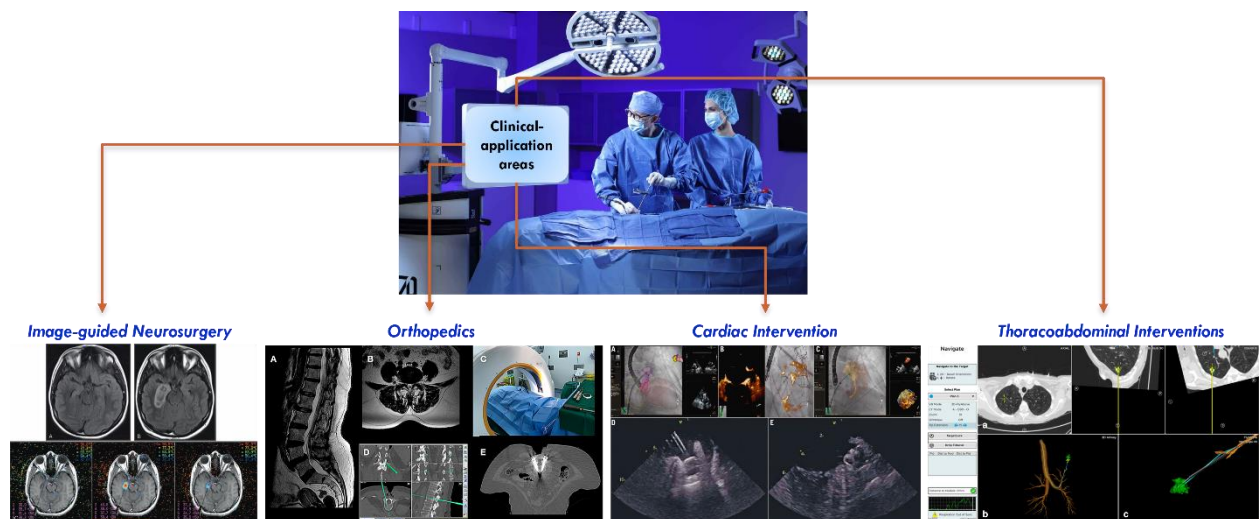


Figure 1-1: Common applications of IGS [4], [5], [6], [7].

Neurosurgery is a specialized field of medicine focused on the diagnosis and treatment of disorder affecting the nervous system, including the brain, spinal cord, and peripheral nerves

[8]. Some clinical examples of neurosurgical procedures where IGS is commonly used are brain tumor resection, deep brain stimulation surgery, epilepsy surgery, intracranial aneurysm clipping, spinal fusion surgery, and functional neurosurgery.

The main objective of brain tumor surgery is to achieve gross total tumor removal without postoperative complications or permanent new disabilities [9]. In brain tumor resection procedures, before treating the brain tumors, neurosurgeons use preoperative MRI or CT images to build accurately 3D models of the tumor and surrounding brain tissues. During the surgery, the surgeons use navigation system to ensure that the tumor is precisely targeted and removed with minimal risk of damage to healthy surrounding brain tissues. Some different approaches commonly used in IGS-based surgeries for brain tumor resection such as craniotomy, endoscopic surgery, and keyhole surgery [9].

For epilepsy treatment, although open resection surgery is still the main treatment approach, it is often considered the last option because of its invasiveness [10]. Therefore, minimally invasive surgical approaches under assisting of IGS promise an improved way in modern epilepsy surgery. IGS supports neurosurgeons in precisely locating the neurological treatment regions by registering preoperative images to intraoperative images. This reduces the possibility of postoperative neurological effects and ensures that the resection region is accurately targeted. An example of image-guided diagnosis and resection epilepsy surgery by co-registration between the T1-weighted images and T2-weighted or the fluid-attenuated inversion recovery (FLAIR) images for fifty patients shows promised results for intraoperative identification of otherwise poorly visible lesions on standard MRI sequences in good spatial resolution [11].

Orthopedic surgery remains technically demanding due to the complex anatomical structures and cumbersome surgical procedures. The development of image-guided orthopedic surgery (IGOS) has substantially decreased surgical risk and enhanced the outcome of the surgical procedure because the IGOS solved challenges and risky possibilities of orthopedic surgery related to the density of muscle tissues, ligaments, blood vessels, and nerves around the operation area [12]. The IGOS focused on addressing two main stages of orthopedic surgery including preoperative planning and intraoperative execution. For planning in the preoperative stage, the IGOS systems provide segmentation and 3D visualization of bones and related structures from patient medical images. The IGOS system provides real-time guidance during the intraoperative stage by presenting the location and orientation of surgical tools about the patient following image registration and surgical tool calibration. Moreover, the integration with augmented reality (AR) and robotics improves the accuracy and automation of the navigation system [12].

Cardiac Image-guided intervention involves the use of advanced imaging techniques and real-time guidance to perform minimally invasive procedures on the heart and its associated structures such as replacement or repair of a malfunctioning valve, restoration of myocardial perfusion by inserting a stent, or grafting an obstructed vessel, or electrical isolation of tissue regions that give rise to arrhythmia [13]. Two cardiac image guidance platforms here present different contexts of using medical images and visualization systems to support surgeons in cardiac interventions. The first platform is a model-enhanced ultrasound-assisted guidance platform developed at the Imaging Research Laboratories (Robarts Research Institute, London, ON, Canada), and the second one is a prototype system for advanced visualization for image-guided left atrial ablation therapy developed at the Biomedical Imaging Resource (Mayo Clinic College of Medicine, Rochester, MN, USA).

The first system integrates magnetically tracked trans-esophageal ultrasound (US) imaging for real-time visualization to allow the interpretation of 2D intra-operative US data within the 3D context that is provided by the preoperative electro-anatomical models within a virtual reality environment. In the context of ablation therapy, virtual reality-enhanced US guidance reduces the risks associated with fluoroscopic imaging and enables the mapping of dynamic EP data onto the preoperative cardiac models. The clinicians can investigate the intracardiac environment and use surgical instruments that is intrinsic to the heart's structure by using registered pre-operative models as a reference [13], [14].

The second platform is built on an architecture that integrates data from left atrial electrophysiology, intraoperative imaging, preoperative imaging, and real-time ablation catheter positioning into a user interface. This interface shows a surface-rendered, patient-specific model of the left atrium and related pulmonary veins segmented from a preoperative contrast-enhanced CT scan along with points sampled on the endocardial surface with the magnetically tracked catheter. These parts are integrated into a surface-based registration, and the model-to-patient registration is updated continuously [13], [15], [16].

Thoracoabdominal interventions under image guidance have emerged slowly because of the difficulty in dealing with the deformable nature of the organs in the abdominal region. Improvements in tracking technologies that its ability is designed to follow instruments inside the body using electromagnetically monitored sensors, have made it possible to do clinical research on organs such as the kidney, liver, and lung [1]. Tumor ablation in the soft tissues of the abdomen and thorax as well as minimally invasive biopsy procedures are frequently performed with the use of image guidance to direct the needle's insertion through the skin and into the target tissues [17]. Over the years, numerous technologies have been developed to improve the process of CT- and/or MRI-guide needle. These systems range from basic passive aids to completely automate robots such as the needle navigation systems ActiViews CT-Guided and CAScination CAS-ONE, the laser reference systems Neorad SimpliCT and Amedo LNS, the patient-mounted AprioMed Seestar, the Light Puncture Robot and Robopsy, the table-mounted AcuBot, the floor-mounted Perfint ROBIO and MAXIO, and various articulated robotic arms [17].

Natural Orifice Transluminal Endoscopic Surgery (NOTES) is the next revolution in minimally invasive surgery because it can reduce the number of incision-related problems, including wound infections, incisional hernias, postoperative pain, and adhesions. Moreover, NOTES is the most suitable approach for patients who are morbidly obese or have obstructive carcinomas, and the conventional surgical approach makes it difficult to access the intraabdominal organs through the abdominal. NOTES employs real-time tracking of the endoscopic camera to represent some intraabdominal structures and to remove inverted images due to these structures might be behind the instruments and only be visible to the scope when it is retroflexed. By registering preoperative (CT, MRI) and intraoperative (US) images with the view through the NOTES endoscope, image-guided developments assist the NOTES to precisely delineate and locate treated regions. Additionally, while the AR techniques guides surgeons to see through structures to identify anatomy and pathology, up-to-date registration algorithms have presented improved interpretation of endoscopic US images in robot-assisted laparoscopic surgeries [1].

1.1.3. Framework of Image-guided surgery

Figure 1-2 depicts a typical framework of image-guided surgery that includes the following steps:

- Preoperative images acquiring
- Patient-specific model generating
- Making surgical planning
- Tracking patient anatomy using tracking system (such as Optical Tracking System, Electromagnetic Tracking System)
- Registering patient's actual anatomy to patient-specific model
- Surgical execution under image guidance.

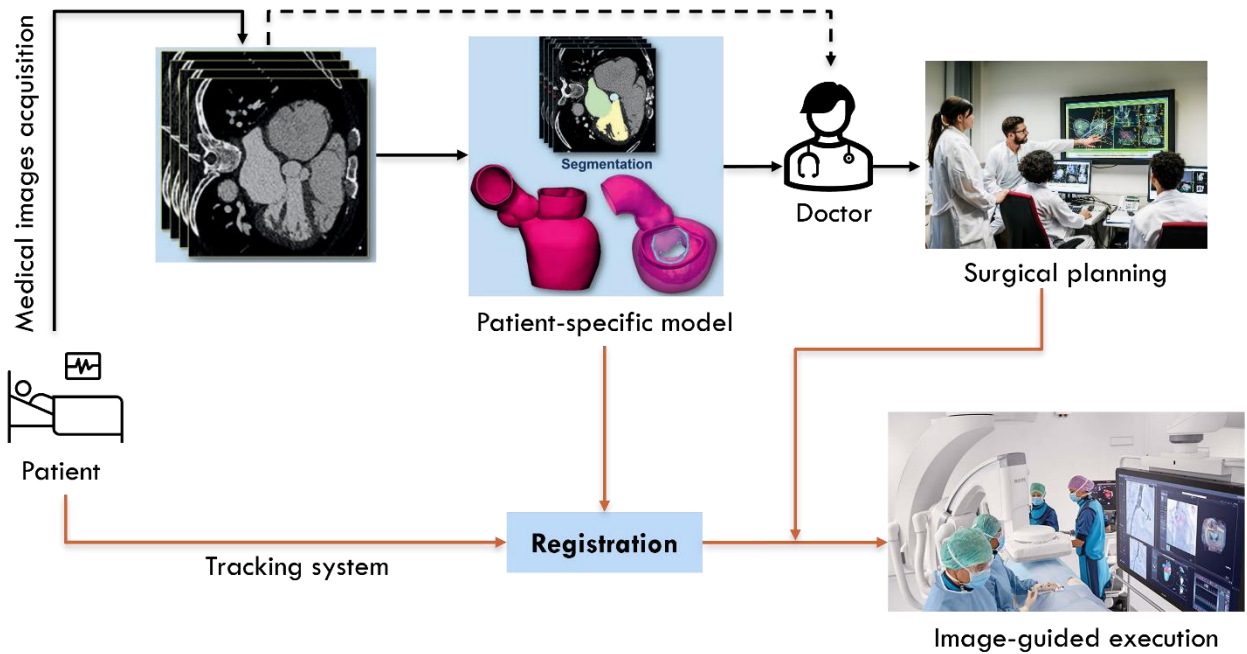


Figure 1-2: Image-guided surgery framework.

The process will begin with preoperative planning where medical images (such as CT, MRI, US) are obtained from the patient. The need-to-be-treated region or the disease region is segmented from the preoperative images and then generated into 3D models using specialized software (such as 3D Slicer [18]). This model is called patient-specific model. The preoperative medical images and the patient-specific model provide substantially anatomical information about the patient's body and disease region to be treated, allowing surgeons to visualize detailly and make a surgical plan for the surgery.

The tracking system is used to track the position of instruments relative to patient anatomy. Early tracking devices were essentially mechanical digitizers, and the optical or magnetic spatial localization systems, depending on the application, are employed to identify the position and orientation of the surgical instruments [13]. Next, the intraoperative coordinates defined by the tracking system need to be registered to the patient-specific model. This process ensures that the patient-specific model and the real-time coordinates are in the same coordinate system, enabling accurate surgical navigation and interventions. The registration starts with an initial alignment determined by landmark identification. Anatomical

landmarks in both the preoperative model and the intraoperative coordinates are identified correspondingly around the region of interest (disease region or the need-to-be-treated region), then using these landmarks to establish an initial alignment between the patient-specific model and the intraoperative coordinates. The initial alignment could be utilized by using point-based registration (applying to pairs of corresponding points), or surface-based registration (applying to the surfaces of anatomical structures) [19]. An iterative closest point (ICP) algorithm is then used for fine-tuning the alignment by minimizing the distance between corresponding points on the patient-specific model and the intraoperative coordinates iteratively [19].

1.2. Dissertation outline

The work provided in this dissertation that acknowledges the potential of image registration and automatic surgical planning to improve the effectiveness of preoperative planning and intraoperative process leading of image-guided surgery, discusses the following thesis statement “Research on automatic surgical planning and registration for Image-guided surgery”.

Three major themes are advanced throughout the dissertation and constructed as following:

- (i) Chapter 2 presents a framework for multimodal image registration in the preoperative process using a feature-based approach and image segmentation assistance is proposed to achieve complementary information from CT and MRI images. The surgical context is applied to the region of interest of the liver with 24 pairs of CT-MRI images.
- (ii) Chapter 3 reports a computer-assisted surgical planning method using novel forms of statistical shape models generated by Shapeworks and ANTs (Advanced Normalization Tools) and applied in a clinical scenario of humerus datasets to establish a framework for automatic surgical planning in the preoperative stage.
- (iii) Chapter 4 provides a proposed markerless registration framework using a dynamic touchable region model for intraoperative registration. The results are quantitatively evaluated in three different phantoms toward the clinical context. The registration results of the proposed method are also compared to the conventional paired-point registration.

Chapter 2. Feature-based multimodal image CT-MRI registration assisted by segmentation

2.1. Introduction

2.1.1. Related work

Multimodal image registration is a process of mapping spatially anatomical structures from different image modalities to the same coordinates [20], [21], [22]. Since a few decades ago, the multimodal image registration process has been utilized for preoperative surgical planning, intraoperative surgical decision-making, and postoperative. This process could provide precise visualization and delineation of regions of interest (ROI) to differentiate between abnormal and normal tissues, estimate tumor location or being treated regions for clinical procedures with minimal damage [23], [24]. Therefore, this process is a necessary preprocessing step for non-invasive image-guided surgeries such as head and neck tumor treatment planning [25], [26], radioembolization (as known as selective internal radiation therapy SIRT) [27], [28], external beam radiation therapy EBRT for treating prostate cancer [29], [30].

For example, during pre-treatment and post-treatment of the SIRT, certain branches of the hepatic artery are treated with microsphere radiopharmaceuticals, such as [^{68}Ga] DOTATATE-avid or [^{18}F]FDG (fluorodeoxyglucose), both before and after the SIRT to mimic the activity distribution of microsphere in the liver. PET/CT or SPECT/CT can be used to measure the concentration of [^{68}Ga] DOTATATE-avid or [^{18}F]FDG, which is a higher concentration in the tumor cells than in the normal tissues. Then, MRIs are acquired for regions that are not treated by [^{68}Ga] DOTATATE-avid or [^{18}F]FDG. Finally, the distribution of treatment irradiation is then evaluated by registering the CT and MRI images [27], [28].

For instance, during prostate cancer treatment using EBRT, to reduce side effects, the prostate volume should be the focus of the planning stage of EBRT treatment, while the organs at risk such as the bladder and rectum should be spared. After acquiring CT images of the area to be treated, radiation experts would define the gross tumor volume, clinical target volume, and planning target volume on each CT slice for making treatment planning. To evaluate the treatment plan, the surrounding tissues and organs at risk should be annotated. However, because of the low contrast for soft tissues, it is difficult to interpret and clearly identify the prostate, bladder, and rectum on the CT images. Therefore, MRIs are acquired due to the advantages of high contrast on soft tissues. Finally, the MRI is registered to the CT for accurate contour propagation [29], [31].

Therefore, this chapter focuses on tackling the registration of MRI and CT images since it is the most common multimodal medical image registration task. This task could not only combine the superior soft tissue contrast of the MRI with the high spatial resolution and dense tissue contrast of CT for surgical planning [26], [32], but also the CT images could provide the accurate distribution of electrons in tumor regions while the MRIs are utilized for delineating surrounding soft normal tissues in the context of radiation therapy planning [33], [34].

MRI and CT registration is a necessary procedure in the field of medical imaging, where data from both modalities are integrated to improve the accuracy of diagnosis and planning of treatments. However, the challenge of this procedure is the need to tackle the geometric distortion and the intensity distortion. MRI modality is particularly suffered to geometric

distortion due to magnetic field inhomogeneities, gradient nonlinearities, and patient-induced susceptibility effects [35]. In the context of CT, the geometric distortion is caused by patient motion, including variation in positioning, breathing level, and pathological changes [32]. Moreover, the intensity distortion due to the distinct physical principles that underlie MRI and CT imaging modalities [22], [32].

To solve the geometric distortion problem, some algorithms for geometric distortion correction were applied to MRI such as field map-based correction [36], non-linear gradient correction [37], and image-based retrospective correction [38], whereas geometric distortion in CT images could be resolved by using deformable registration for more localized distortions. Field map-based correction algorithms rely on accurately mapping the magnetic field inhomogeneities. However, field maps are affected by noise and errors, especially in areas where susceptibility differences are considerable, such as at the interface between air and tissue. These errors may lead to inaccurate field map-based corrections [36]. Geometric distortion in MRI also could be caused by non-linear gradient distortions. Although, there exists some methods to model the gradient fields and correct these distortion, the accuracy of these methods is limited by the complexity of the magnetic field fluctuations and the quality of the gradient coil characterization [39]. Consequently, the inaccuracy of geometric distortion correction methods applied to MRIs needs to be considered in the process of MRI and CT registration. According to the study in [25], the inaccuracy of the geometric correction could be resolved and the necessity for geometric distortion correction could be eliminated by using deformable registration for MRI and CT registration.

To deal with the challenges of intensity distortion, numerous strategies have been proposed and categorized into three groups: (1) techniques based on information theory, (2) techniques based on features, and (3) techniques relying on image synthesis. The idea for the information-theory-based registration method is to establish an efficient similarity measure that can be used to find correspondences between images with different modalities. Mutual information (MI) and its variants [40], [41], which optimize the quantity of shared information between two images by striving to identify a statistical intensity relationship between them [32], are the most common information theoretic measure in the first category. Despite being successfully and extensively used for the rigid multimodal alignment [41], MI and its variants need to deal with many difficulties for deformable multimodal image registration. The primary disadvantage is that this approach is affected by local intensity variations which can lead to inaccurate local optima in non-rigid registration because the MI is intrinsically a global measure and it is difficult to estimate the intensity histogram with tiny image patches [31], [32], [42]. Furthermore, the spatial information and anatomical information are completely ignored because the conventional similarity measure only considers the intensity histogram information [31], [42].

The idea of the third category, on the other hand, comes from that the challenge of multimodal image registration could be simplified to monomodal image registration by using the image synthesis technique. The fundamental concept is that by synthesizing one modality from another, a significant appearance gap between two different modalities could be narrowed. Consequently, this allows for the direct registration of two visually similar images using the conventional deformable registration method [31]. Several image synthesis methods have been proposed and divided into two categories to reach the goal of generating one image modality from other image modalities. The first category is exemplar-based image synthesis, and the second category is learning-based image synthesis [29], [43]. For the exemplar-based image synthesis approach, the new source image can be sparsely represented by patches from an atlas

dataset of the same modality, the target image patches of a different modality can be predicted using the computed sparse coefficients. However, due to expensive optimization, the prediction process can become completely computationally costly, and incorrect predictions could occur in noisy synthesized images [29], [43]. Additionally, the target modality's image can be synthesized using the learned model, which was developed by the Gaussian mixture regression model [44], [45], random forest regression model [29], [31], [43], and deep learning model [26], [46]. While these studies have shown positive results in the synthesizing MRI to CT or vice versa, the learning-based method has limitations such as prolonged training duration, extensive training data requirements, and its performance heavily relies on the proper tuning of many parameters [31], [43]. Conclusion, the quality of the synthesized image will affect the registration accuracy, which must be guided by precise anatomical alignment. Furthermore, integrating complementary data from different modalities for precise and reliable multimodal image registration remains a difficult task in image-synthesis-based multimodal registration [29], [31].

Several multimodal registration methods based on features have been proposed to establish correspondence by exploiting high-order appearance information, such as geometric moments [47], histogram of oriented gradient (HOG) [48], Gabor attributes [49], scale invariant feature transform (SIFT) [50], and gradient location and orientation histograms [51]. These methods showed promising results for feature-based multimodal image registration but it is challenging to determine helpful features that both indicate common anatomical details and are invariant to appearance differences [29]. Another neighborhood descriptor that is independent of modality (MIND) [32] was proposed based on the self-similarities in the neighborhood to provide distinct correspondences across different modalities. Although the effectiveness of MIND is improved in cases where there is consistency between the local anatomical feature and structural patterns in small neighborhood, the robustness of MIND needs to be considered when the local anatomical variance increases notably [31].

Although it is difficult to extract an effective and modality-independent feature applying for multimodal image registration, feature-based approaches have been widely used for both general monomodal and multimodal image registration in the field of medical imaging research [20]. In comparison to intensity-based approaches and image-synthesis-based approaches, feature-based approaches are simpler and need less computing work. For many clinical scenarios, the feature-based approaches provide an appropriate alternative when features such as organ boundaries can be determined with minimal or no participation from the user [20]. In recent years, with the development of automatic, well-validated, and learning-based techniques for medical image segmentation, feature extraction method has improved rapidly [52], [53]. Additionally, some segmentation-based methods combine the segmentation and registration procedures [54], [55], whereas others utilize segmentation results to improve multimodal registration by adding an auxiliary loss function that leveraging anatomical segmentation at training time [56], or to identify correspondences between different imaging modalities in a weakly-supervised framework [22], or to learn image features on a supplementary segmentation task and drive the optimization of a registration model [57]. Therefore, using medical image segmentation is a promising research direction to assist an accurate feature-based multimodal image registration.

The significance of feature-based multimodal image registration assisted by segmentation is in the requirement of (1) a precise segmentation method and (2) a feature extraction method with effectiveness, modality-independence, and spatial information presentation to achieve accurate non-rigid registration. Due to manual medical image

segmentation is a laborious task that is time-consuming and relies heavily on the expertise of radiologists or experts, leading to a lack of reproducibility and variability among different experts [58], [59], an automatic method for medical image segmentation is required. There are numerous effective methods for medical image segmentation with a diversity of anatomical regions such as neuroanatomy [60], liver and its vessels [61], a group of brain ventricles, retina nerve, and liver [62], a group of abdominal organs including liver, kidney, and pancreas [63], and so on, but this chapter mainly focuses on methods that deal with liver segmentation applications. It is because the purpose of this chapter is establishing a framework for CT-MRI registration applied to liver region. Additionally, to alleviate the complexity of the segmentation procedure, this chapter also expects the segmentation methodologies suitable for usage with CT and MRI.

An automatic segmentation method that is independent of modality and has the capability to automatically track the longitudinal liver volume from various scans has the potential to provide valuable prognostic information [64]. The idea of the modern independent-modality segmentation methods is the learning-based approaches, such as an anatomy-preserving domain adaptation to segmentation network (APA2Seg-Net) [59], KiU-Net [62] as a combination of an overcomplete architectures Kite-Net (Ki-Net) and an undercomplete U-Net, a cascaded fully convolutional neural networks (CFCNNs) [65], a generalized convolutional neural network [64], and nnU-Net [66].

The APA2Seg-Net consisted of (1) the anatomy-preserving domain adaptation network (APA-Net) to adapt images from the conventional CT domain to the CBCT/MRI domain and the inverse way, and (2) a segmentation network to predict the liver region without target modality ground truth [59]. Although the APA2Seg-Net showed some positive segmentation results for CT and MRI datasets, some potential limitations need to be considered. The APA2Seg-Net was only implemented with the 2D networks because the amount of training data was not large enough to train with a robust 3D network. While the use of 2D flexibility elements, for example, generator, discriminator, or segmenter, could not claim optimality of the combination for segmentation, the imperfect segmentation results could lead to inaccurate registration results [59]. The KiU-Net proposed an architecture for capturing fine details and accurate edges and learning high level features on the input applied to different modalities such as MRI, CT, US, but its application focused on precisely small masks and finer details of surfaces and edges [62]. Although the liver segmentation method using CFCNNs or the generalized convolutional neural network, which was proposed to solve the disadvantage of CNN in the requirement of a large amount of manually label data for the training process, presented impressive liver segmentation results with Dice scores higher than 0.9, these approaches always need to apply image preprocessing methods suitable for each different modality imaging, such as [65] applied HU windowing for CT and N4 bias correction for MRI, or contrast-enhanced images in the study of [64]. The most impressive neural architecture is the nn-UNet with extremely effective implementation to (1) adapting to any new dataset, (2) handling a wide variety of target structures and image properties, (3) outperforming specialized pipelines in a range of diverse tasks, and (4) displaying strong generalization characteristics requiring neither expert knowledge nor computing resources beyond standard network training [66]. Based on the discussion of the advantages and disadvantages of the aforementioned methodologies, the nnU-Net and its trained models were selected for the purpose of liver segmentation in this chapter.

For the requirement of expecting a feature extraction method to fulfill the conditions of effectiveness, independent on modality, and providing spatial information of the region of

interest, the textural features and their variants are considered in this chapter. The first definition of textural features is that contain information about the spatial distribution of tonal variations within a band, published in [67], 1973. The study of [67] provided an understanding of the relation between the structure of surfaces and their interactions with their surroundings by presenting textures as a spatial distribution of gray tones (in a gray image). The 13-dimensional texture features that were defined in [67] could be briefly called Haralick features. Haralick features identify patterns of gray-level co-occurrence, which are then utilized to build a matrix of co-occurring gray-level pairings within the image. It is possible to calculate second-order statistical texture features with this matrix. Haralick texture analysis is rather popular in the field of medical image analysis especially for classification-related applications since it uses second-order intensity statistics (such as angular second moment, contrast, and differential entropy) to capture variations in gray-level image features. However, Haralick features may be resisted by small variations in sub-structures that have the same co-occurring gray-level intensities but differ morphologically [68]. To solve this problem, the study in [68] proposed a new descriptor of Co-occurrence of Local Anisotropic Gradient Orientations (CoLIAGe) to determine the entropy of co-occurrences of pixel/voxel-level gradient orientations established inside a local neighborhood in order to quantify the local anisotropic variations in micro-structures. The results of [68] demonstrated that CoLIAGe had a much greater classification accuracy than the Haralick and the expert readers for both CT and MRI in three cases of brain tumors, breast cancer, and adenocarcinomas from granulomas. However, the application of the CoLIAGe was limited to classification and had not yet been utilized for registration.

2.1.2. Contribution

The purpose of this chapter is to merge region-of-interest segmentation results with spatial features obtained from the ROI to achieve enhanced results in multimodal image registration applied in CT and MRI. The CT and MRI datasets displayed the anatomical structures of the abdomen with particular emphasis on the liver region.

In the domain of liver registration, several studies have been conducted focusing on registering CT and MRI images using segmentation results as a guiding framework. Examples of such studies include the research by Xikai Tang *et al* [27] and the study by Bo Zhou *et al* [59]. The research by Xikai Tang *et al* employed segmentation results as a segmentation similarity loss function within the final loss function to evaluate the non-rigid registration procedure [27], whereas the study by Bo Zhou *et al* extracted surface points from the CBCT and MRI segmentations and input these points into the Robust Point Matching to estimate the multimodal registration transformation [59]. Although these studies presented some positive registration results, the approaches of these studies did not involve image features or deformable registration algorithm. As per the comprehension, this chapter marks the initial exploration that uses segmentation results and CoLIAGe features for multimodal image registration. The procedure begins by utilizing nnU-Net to segment the liver regions in CT and MRI images, and extracts CoLIAGe features in CT and MRI images as the descriptor images from the liver regions, consequently. As a result, the descriptor images are registered by applying a Symmetric Normalization (SyN) deformable algorithm [69].

2.2. Materials and Methods

A three-stage multimodal image registration framework for mapping the MRI image to CT is presented in Figure 2-1.

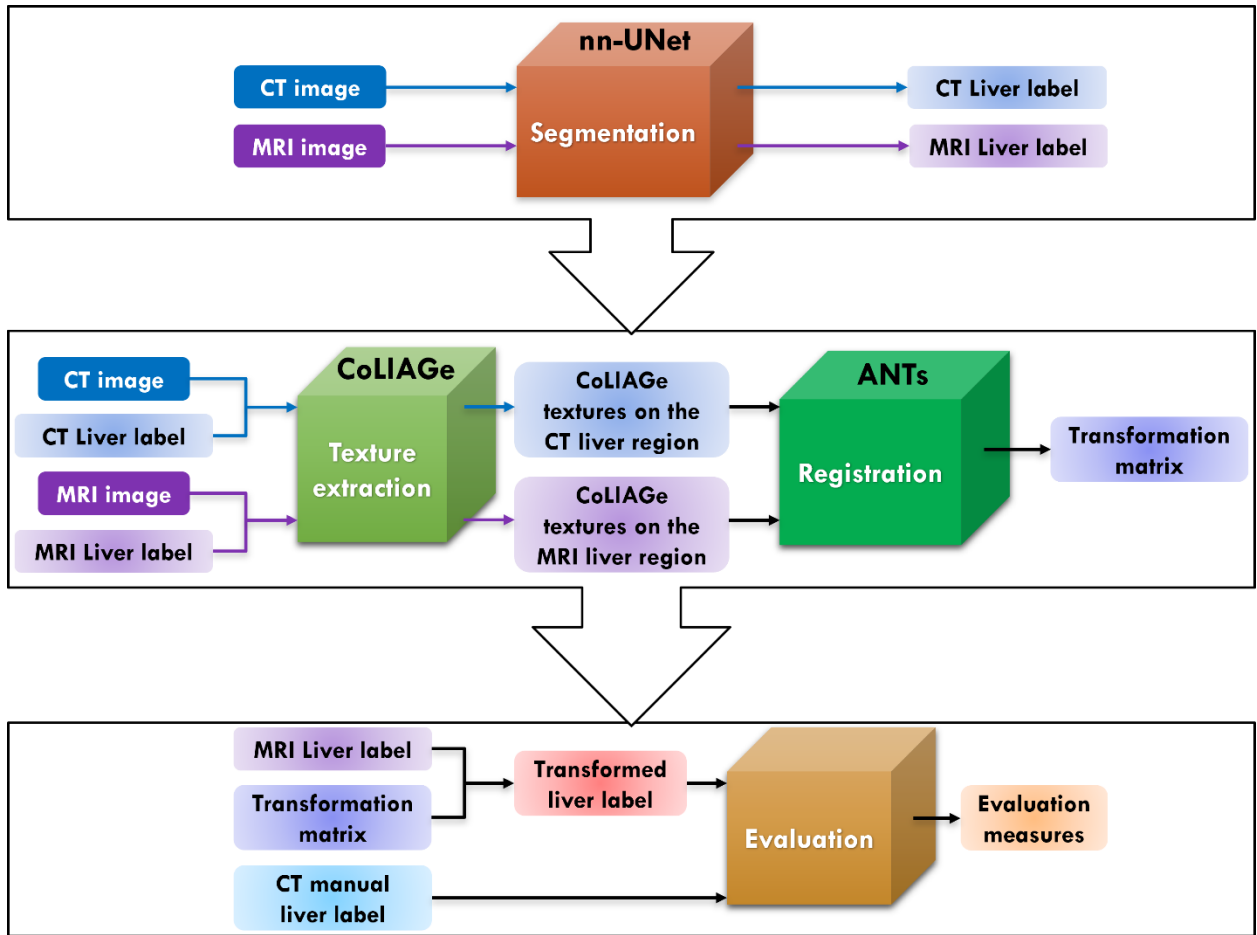


Figure 2-1: The proposed framework of MRI-CT multimodal image registration.

In the first stage, the liver regions in the CT and MRI images were segmented by using the nnU-Net. The datasets of CT and MRI consisted of a collection from Kyungpook National University Hospital and two parts from two open datasets CPTAC-CCRCC and CPTAC-PDA, and were detailed in Table 2-1 and Table 2-2. The 3D full-resolution nnU-Net model, which was applied to CT segmentation in this chapter, was available in the study [66] by training the dataset of The Liver and Liver Tumor Segmentation Challenge (LiTS) with 131 training CT images with ground truth annotations for the liver [70]. In contrast, for MRI segmentation task in this chapter, the 3D full resolution nnU-Net was made accessible in the study of [66] by training 60 MRIs from Task 5 multiorgan segmentation of the Combined Healthy Abdominal Organ Segmentation (CHAOS) Challenge [71].

Table 2-1: Detailed information of CT and MRI images used for multimodal registration

Dataset	Patient ID	CT image ID	MRI image	
			ID	Modality
	Patient 1	CT1	MR1	T1
	Patient 2	CT2	MR2	T1
	Patient 3	CT3136140	MRI3136140	T1

Kyungpook National University hospital	Patient 4	CT3368799	MRI3368799	T1
	Patient 5	CT3635608	MRI3635608	T1
	Patient 6	CT3636884	MRI3636884	T1
	Patient 7	CT3650147	MRI3650147	T1
	Patient 8	CT3661039	MRI3661039	T1
CPTAC-CCRCC https://wiki.cancerimagingarchive.net/pages/viewpage.action?pageId=33948213	C3L-00610	C3L00610_10032_5	C3L00610_5	T2
			C3L00610_6	T2
			C3L00610_9	T2
			C3L00610_14	T2
CPTAC-PDA https://wiki.cancerimagingarchive.net/pages/viewpage.action?pageId=33948258	C3N-02010	C3N02010_2	C3N02010_3	T2
		C3N02010_3		
		C3N02010_4	C3N02010_17	T1
		C3N02010_5	C3N02010_22	T1

Table 2-2: Statistics about the CT and MRI datasets

Specification	CT	MRI
Number of sets	13	15
In-plane spatial resolution [number of sets]	512 x 512 [11]	512 x 512 [9]
	766 x 512 [1]	256 x 216 [1]
	588 x 512 [1]	512 x 432 [2]
		640 x 520 [3]
Number of axial slices in each examination [min – max]	[45 – 399]	[33 – 124]
Total axial slice number	2610	1476
Left-right spacing (mm/voxel) [min – max]	[0.54 – 0.81]	[0.59 – 1.41]
Anterior-posterior spacing (mm/voxel) [min – max]	[0.54 – 0.81]	[0.59 – 1.41]
Slice thickness (mm) [min – max]	[1 – 5]	[1 – 7.2]

Because the 3D full-resolution nnU-Net for MRI segmentation task in this chapter was trained from multiorgan segmentation task including the liver, the spleen, and the left and right kidneys segmentation, a postprocessing step was conducted to extract the liver region as the largest region among five outcome labels. As a result, the output of the first stage was the liver label images corresponding to the CT and MRI. Note that the 3D full resolution nnU-Net for CT segmentation and MRI segmentation are available at [66].

The registration stage comprises of two parts: the initial step involves extracting texture features, followed by the step of deformable registration using ANTs. After obtaining the liver labels from the first stage, pairs of CT image and corresponding liver label image, MRI and corresponding liver label image were fed into the step of extracting the CoLiAGe features as described in the study of Prateek Prasanna et al [68]. It should be considered that the full CoLiAGe features are 13-dimensional vectors, therefore there are 13 kinds of descriptor image including angular second moment, contrast, correlation, entropy, and so on. However, the entropy descriptor was extracted for registration in this chapter based on the empirical comparison of the registration accuracy using 13 kinds of descriptors. Inputs for registration step are CoLiAGe entropies of the liver regions from the CT and MRI, and the registration method was the SyN algorithm in ANTs because this algorithm demonstrated the most consistently high accuracy registration across subjects in a comparison of 14 nonlinear deformation algorithms [72]. After the registration process was completed, the transformation matrixes were preserved for the subsequent stage of evaluation.

The evaluation stage is illustrated in the bottom part of Figure 2-1. The manual liver labels were corrected by an expert from the Kyungpook National University Hospital and served as the ground truth for the evaluation. This chapter evaluates the segmentation stage and registration accuracy using evaluation measures as explained in a study by Tobias Heimann *et al* [73]. The measures consist of the Dice similarity coefficient, Jaccard coefficient, Volumetric overlap error, Relative volume difference, Average symmetric surface distance, and Maximum symmetric surface distance. However, this chapter focused on the Dice similarity coefficient and the Average symmetric surface distance.

2.3. Results

2.3.1. Segmentation results

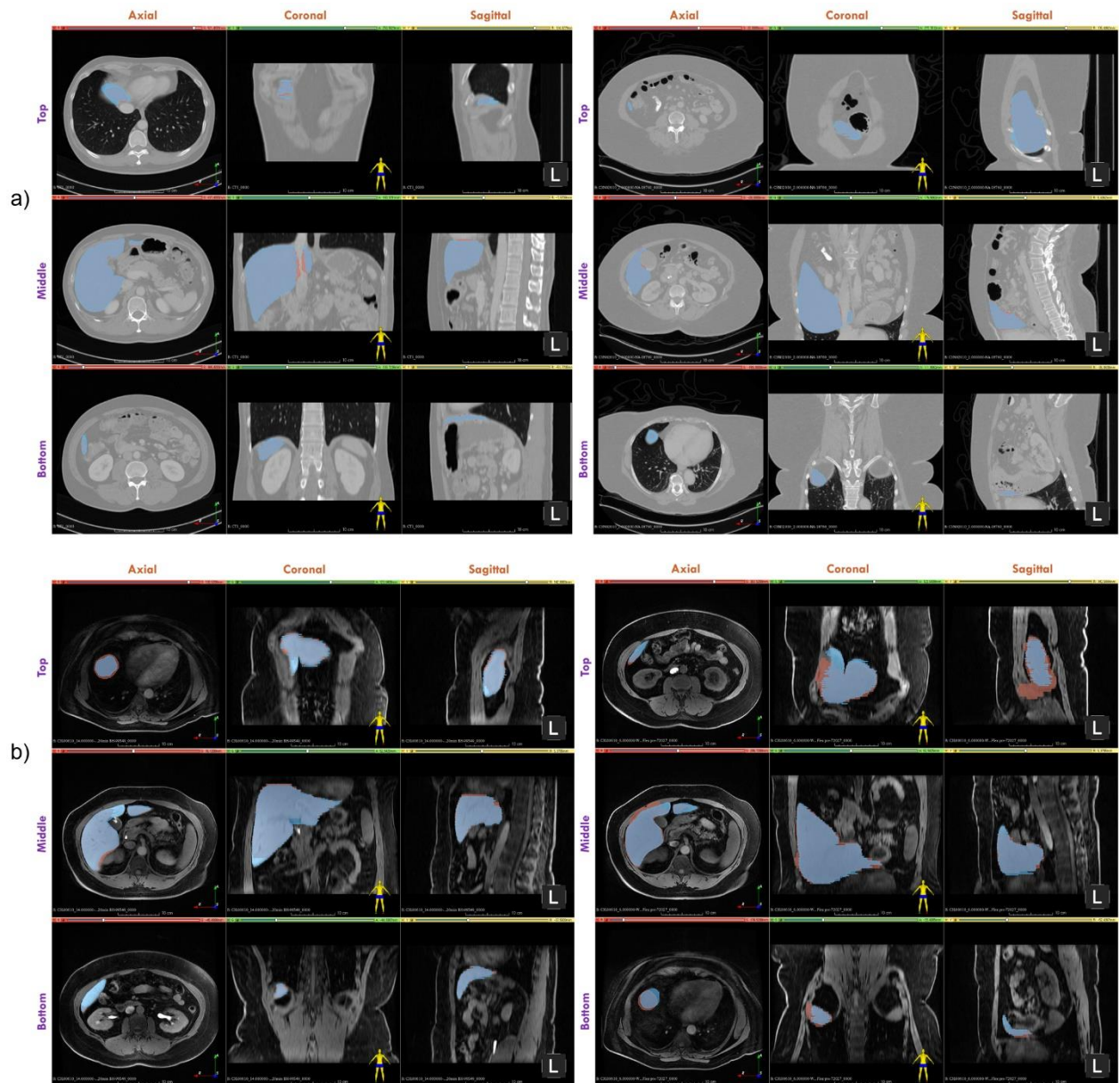


Figure 2-2: Comparison between manually segmentation and nnU-Net-based segmentation at different liver latitudes for different patients. Red mask: liver segmentation predicted by nnU-Net; Blue mask: liver segmentation ground truth.

The segmentation results serve as the guiding framework for feature extraction and registration, therefore the qualitative analysis for segmentation needs to be considered. A comparison between the qualitative results of CT segmentation and MRI segmentation at different levels of liver scans for different patients is illustrated in Figure 2-2. Segmentation results could be readily observed to closely approximate the ground truth, particularly results in the CT segmentation (Figure 2-2a) across all liver latitudes. Conversely, the MRI segmentation results in Figure 2-2b showed ideal segmentation at middle latitudes but slightly differed from the ground truth in the upper liver latitudes. Despite the liver slices being obtained

in an atypical orientation in certain cases (second column of Figure 2-2) in both CT and MRI, the segmentation results exhibited satisfactory performance.

Figure 2-3 displays the Dice similarity coefficient between the nnU-Net liver segmentation of CT and MRI images and the liver ground truth. The average Dice coefficients for CT and MRI images are approximately 0.958 and 0.759, respectively with a note that the Dice coefficient will be 1 for a perfect volume overlap [73]. The highest and lowest Dice coefficients for MRI segmentation are 0.934 and 0.398, respectively, while the corresponding values for CT segmentation are 0.974 and 0.934.

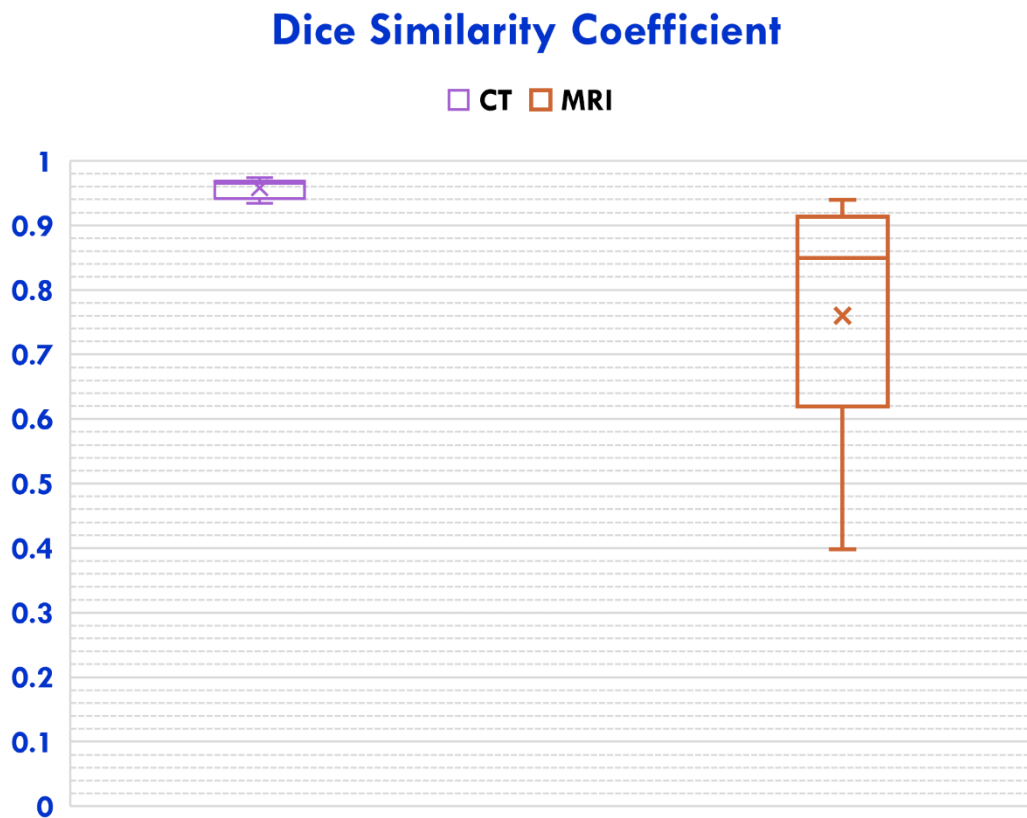


Figure 2-3: Dice similarity coefficients between liver segmentation ground truth and nnU-Net liver segmentation prediction of 13 CT and 15 MRI images.

2.3.2. Registration results

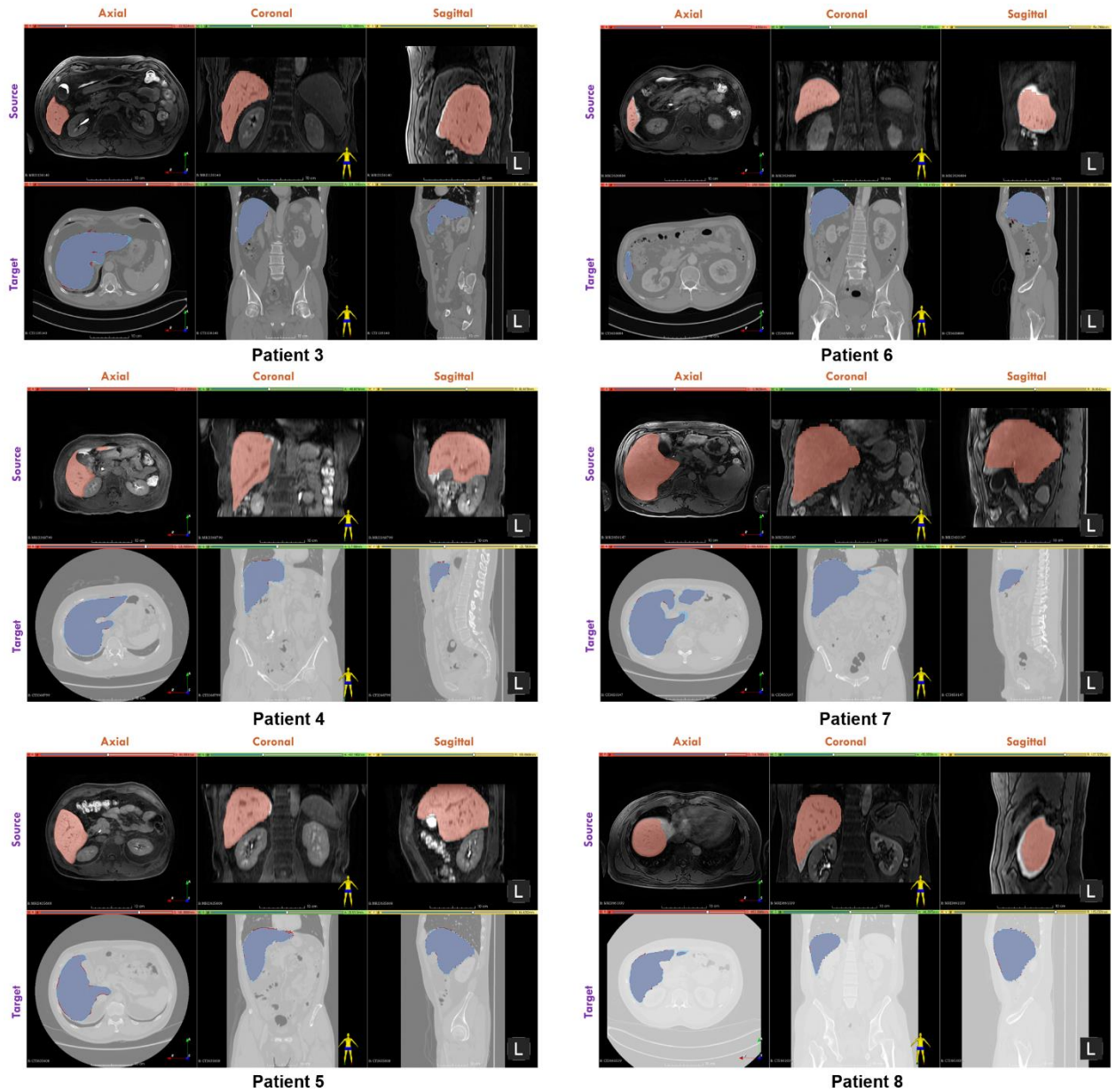


Figure 2-4: Overlaid registration results with CT (target) and MRI (source). Source: Red color presents liver segmentation prediction using nnU-Net for MRI; Target: Blue color presents CT liver ground truth, Violet color presents overlap between the registered MRI liver mask and the CT ground truth.

Figure 2-4 presents the overlaid registration results to qualitatively evaluate the registration performance with CT served as target and MRI served as source image. The red color regions of the source images represent the liver segmentation prediction generated by the nnU-Net. In contrast, the target images show the blue regions representing the CT liver ground truth, and the violet regions denoting the region of overlap between the registered MRI liver mask and the CT ground truth. The overlaid results demonstrate that the utilization of the proposed framework for registering MRI to CT provided transformed masks that closely resembled the ground truths for all patient scenarios.

The Dice similarity coefficient and the Average symmetric surface distance (ASSD) between the human annotated CT liver segmentation and the transformed MRI liver segmentation using the proposed framework were computed and shown in the Figure 2-5. Most ASSR representing red rhombus points are nearly 0, while all Dice coefficients representing blue circle points are higher than 0.8 across all 24 pairs of CT-MRI registration. It needs to be noted that the ASSD is given in millimeters and a volume overlap is perfect if the value of ASSD is 0 [73].

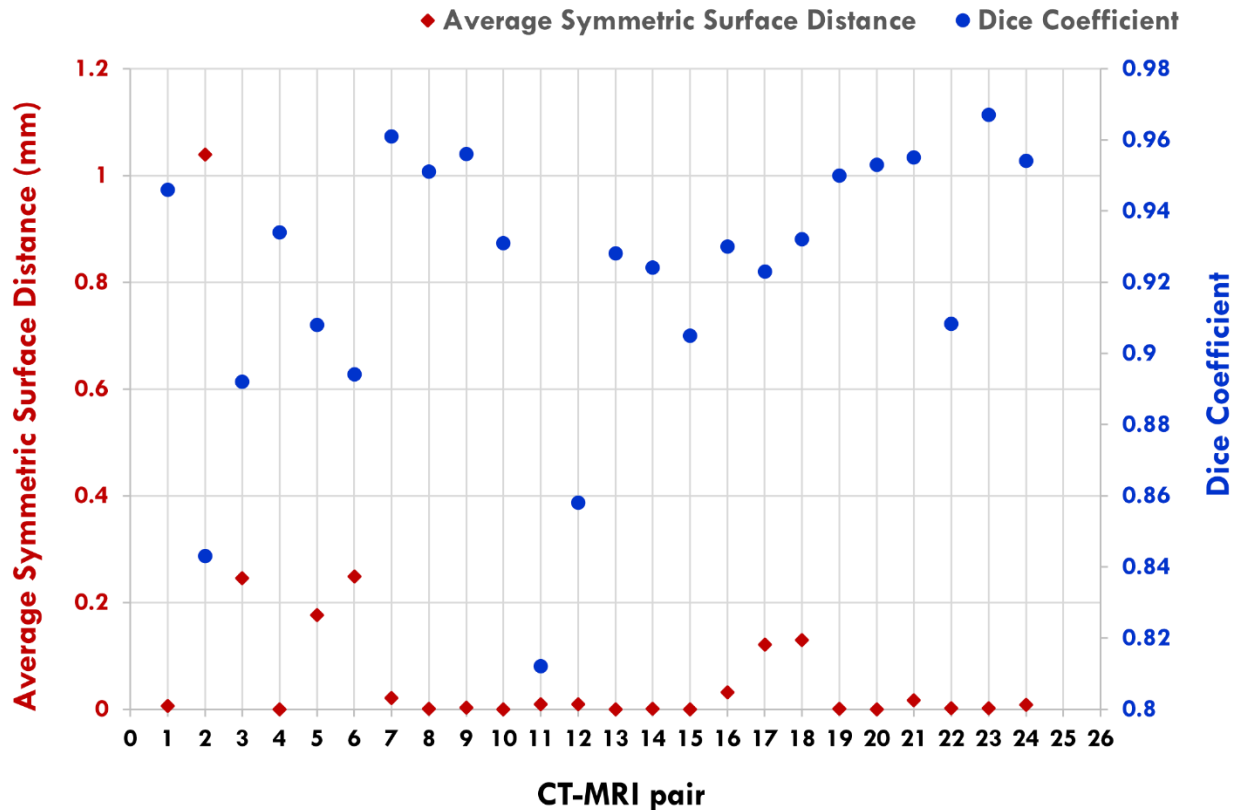


Figure 2-5: Registration evaluations presented by Dice coefficient and Average Symmetric Surface Distance.

2.4. Discussion and Conclusion

To execute the main idea presented in this chapter, the liver region was first automatically segmented for both CT and MRI using the nnU-Net. Subsequently, the CoLIAGE method was used to extract the significant spatial features of the liver regions for both CT and MRI and represent CoLIAGE features as descriptor images. These descriptor images were then registered using ANTs SyN deformable method.

Figure 2-3 illustrated the segmentation performance using the nnU-Net trained models for CT and MRI datasets. It is recognized that the performance of CT segmentation is notably superior to that of MRI, as indicated by a higher Dice coefficient of 0.958 ± 0.0130 for CT and 0.759 ± 0.177 for MRI, respectively. These results could be explained by two reasons. The main reason is segmentation from MRI can be considered a more challenging task in comparison to segmenting CT image because CT images have a typical histogram and dynamic

range defined by Hounsfield Units (HU), whereas MRIs do not have such a standardization [71]. Additionally, the difference in CT and MRI segmentation could be correlated to the lower resolution and higher spacing of the MRI dataset than the CT dataset as detail presented in Table 2-2, and this could lead a higher spatial error for each misclassified voxel [71]. Another reason could relate to the training process of liver segmentation for CT and abdominal organs segmentation for MRI in the nnU-Net. The liver segmentation model for CT was trained on the LITS dataset with 131 training cases, while the amount of training data for abdominal organs MRI was limited with 60 training cases of the CHAOS dataset including modalities of T1 in phase, T1 out phase, and T2.

In summary, a new approach for feature-based multimodal image registration for CT and MRI images was presented in Chapter 2. This approach used nnU-Net, an effective segmentation technique, to determine the region of interest (ROI) from both CT and MRI data. The significant spatial features of the ROI from both CT and MRI were then extracted by using CoLIAGes as independent descriptor images, and next descriptor images were registered by the deformable SyN algorithm of ANTs. The incorporation of segmentation into the registration pipeline ensured that the resulting transformation accurately reflected the anatomical correspondence, leading to better spatial alignment. This approach demonstrated significant improvements in registration accuracy and computing efficiency, establishing the path for more effective integration of multimodal imaging data in clinical diagnosis and treatment planning.

Chapter 3. Feasibility study for the automatic surgical planning method based on statistical model

3.1. Introduction

3.1.1. Related work

Preoperative procedures such as surgical target identification, surgical access planning, and surgical instruments and implant positioning are surgical-supported fields of computer assisted surgical planning [74]. It effectively assists surgeons in making clinical decisions and improving surgery outcomes in a variety of surgical specialties including orthopedic [75], cranio-maxillofacial [76], [77], neurosurgery [78], [79], [80], and so on.

Studying interpatient variability is crucial for surgical planning because individual variations in the shape analysis of anatomical structure can affect significantly the outcome of typical surgeries, such as head and neck cancer resection [81], orthopedic implants [82], [83], [84], and craniostylosis surgery [85]. Therefore, research on anatomical shape analysis has become an essential component of surgical planning.

More than a century has passed since the beginning of studies on anatomical shape analysis. Using statistical power, statistical shape modeling (SSM) has emerged as a significant advancement in morphometric techniques for precise visualization of complex anatomical structure and their variability in the population [86], [87], [88]. SSM provides two distinct kinds of population data. The first one is the *mean shape* which is the average of all shapes in the population, and the second one is the *variation parameter*, which represents how much the shape can differ between subjects in the population [89]. The SSM results set a high probability on a normal anatomical structure and a low probability on a pathological shape. Consequently, SSM has gained extensive applications in computer-assisted surgical planning, for example, radiotherapy planning [90], orthopedic surgery [91], spring-assisted cranioplasty [92], and cervical adaptive radiotherapy [93].

Building SSM requires a well-defined correspondence technique, and automatically correspondences computing is based on registration between individual involved shapes [89]. We can divide methods for defining correspondence into two groups: groupwise method and pairwise method. These are based on reviews of correspondence techniques by *Oguz et al.* [94] and evaluation and validation of statistical shape modeling tools by *Goparaju et al.* [87], [95].

The groupwise approach mostly developed from the original Point Distribution Model (PDM), which took into account expressing images or objects as a set of points and generating a SSM using Principle Component Analysis (PCA) [96]. Many research projects have been conducted based on the concept of PDM, using open-source or SSM tools for general anatomy analysis. These include Shapeworks, Minimum Description Length (MDL), and Statismo framework.

The Statismo employs probabilistic PCA to interpret the modeled objects and displays the statistical model as a probability distribution [97], whereas the research of *Davies et al.* uses the MDL principle to automatically determine the optimal correspondence between sets of shapes [98]. Shapeworks introduced Particle-based Modelling (PBM), in which point-to-point correspondence between the involved shapes are represented as dynamic particles on the surface of the modeled shapes, and it is possible to directly optimize the positions of these

particles [86]. The Shapeworks 's algorithm of entropy minimization in shape space is a highly significant contribution to correspondence optimization. Its effectiveness has been shown in a variety of clinical applications, such as atrial fibrillation, hip joint FAI pathology, dysplastic hip joint, orthopedics, cardiology, and scapular morphology in Hill-Sachs patients [86], [95].

Eventhough Shapeworks demonstrated the effectiveness and potential for use in clinical applications, the Shapeworks's principle is still based on the idea that point correspondences between involved structures exist clearly. Futhermore, most of modeled objects using Shapeworks are bones with a largely consistent shape across the population. Establishing point correspondences and generating a SSM using point-based technique can be challenging when dealing with complex structures such as heart and vascular systems, or highly variable soft tissue like liver, spleen, kidney [89], [99], [100].

The pairwise approach maps each subject in the population to a predetermined atlas or template using volume-based or surface-based pairwise correspondence [94]. Surface-based pairwise needs the computation of correspondences between the individual samples and a standard parameter space, to which each individual is mapped. The majority of surface-based pairwise studies used a sphere as the standard space, for instance, *Kelemen et al.* proposed a spherical harmonics (SPHARM) [101] and *Styner et al.* expanded a SPHARM-PDM framework to build statistical shape analysis for brain structure [102] or hippocampus in schizophrenia [103]. However, SPHARM-PDM underperformed Shapeworks in evaluation and validation studies for clinical applications [95]. Utilizing a non-parametric representation of shape as a mathematical object – current – to characterize geometrical data using a vector field is another aspect of the surface-based pairwise approach. Correspondences are calculaed in the space of currents using rigid registration. However, the current-based technique primally relies on the spatial of the currents or the scale of deformation [99], [100].

Studies on SSM using volume-based pairwise method have recently shown positive results for human brain [104], [105], cardiac [100], heart [106], and even brain template of non-human macaque [107]. This method is based on the principle that there are no explicit correspondences between the individuals. Instead of stable structures like bones, these structures concentrated on analyzing shape models of soft tissuses, which have dynamic shapes. In contrast to other studies in the field of volume-based pairwise such as FNIRT [108] or DRAMMS [109], the Advanced Normalization toolkit (ANTs) demonstrated precision results in building template with high accuracy in registration [72], [110]. An ANTs template represents the population average of the involved shapes without bias toward any particular individual [104].

3.1.2. Contribution and acknowledgement

The goal of this chapter is to develop a computer-assisted surgical planning method using a humerus dataset consisting of both male and female subjects with completely corresponding left and right bones. The average population models were generated from the humerus dataset, and next the automated computer-assisted surgical planning method was developed based on the average population models. Surgical planning data could be established to each new individual dataset, even though this dataset was not part of the dataset that was used to generate the average population models. To conduct the main idea of this chapter, the ANTs toolkit was applied to build templates and mean shapes generated from Shapeworks were served as references to evaluate and validate the ANTs templates in a clinical context.

The method and results which present in this chapter were reported as parts of a journal article as follow:

- **Hang Phuong Nguyen**, Hyun-Joo Lee, Sungmin Kim, “Feasibility study for the automatic surgical planning method based on statistical model”, *Journal of Orthopaedic Surgery and Research*, 18, 398 (2023). <https://doi.org/10.1186/s13018-023-03870-x> (SCIE).

The work in this chapter was supported by the Korea Medical Device Development Fund, grant number 1711174276, RS-2020-KD000016.

3.2. Materials and Methods

Figure 3-1 presents a framework for building an average population model and using it in surgical planning. The framework consists of the following steps: (1) preprocessing; (2) splitting data; (3) building the average population model; (4) evaluating the average population model before applying it to surgical planning; and (5) validating for the surgical planning.

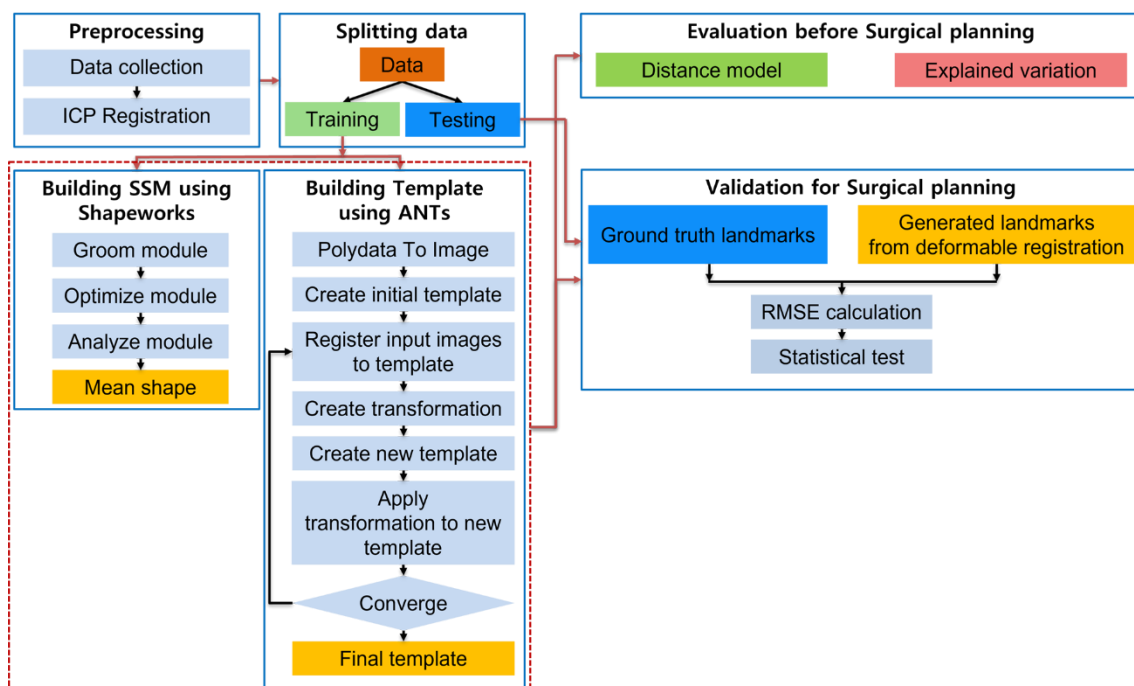


Figure 3-1: Surgical planning framework using the average population model.

3.2.1. Preprocessing and data splitting

The humerus dataset was provided by the Korea Institute of Science and Technology Information (KISTI). The dataset consists of left and right humerus bones collected from 50 female subjects and 43 male subjects. Each file in the dataset was written in STL format. Four sub-datasets were categorized according to gender and side of body. They are male-left, male-right, female-left, and female-right.

The first humerus subject in each sub-dataset was chosen as an initial reference during the data alignment step, and then the Iterative Closest Point (ICP) registration was applied

between the reference and each of the remaining subjects in the sub-dataset. The alignment process was implemented on a 3D Slicer extension developed by our research team.

The training and testing set in each sub-dataset were selected randomly without bias following a ratio of 82% for training and 18% for testing. The training sets were used to build the average population model using Shapeworks and ANTs, while the testing sets were applied for validation.

3.2.2. Building average population model

Shapeworks and ANTs were used to generate the SSM. While SSMs built using ANTs were called templates, those made with Shapeworks were called mean shapes. The process shown in Figure 3-1 applies for each sub-dataset.

To build the SSM, Shapeworks provides an easy-to-use, comprehensive GUI-based interface called Shapeworks Studio. This interface has three modules: groom, optimize, and analyze, as illustrated in Figure 3-1. Because the humerus dataset had already been preprocessed and registered by the ICP algorithm following section 3.2.1, the skipping grooming option was chosen. The optimize module presents options for modeling correspondence dynamic particles between individual subjects using entropy minimization algorithm [86]. After the optimization process was completed, the analyze module extracted the mean shape under polydata format.

A template of ANTs is an unbiased population-average image which respects to shape and appearance from involved individuals [104]. The process for building an ANTs template was shown in Figure 3-1. First, each individual subject was transformed from the original polydata to image using Visualization Toolkit (VTK) [111] to fit the data format required by ANTs. The largest volume image was used as a reference coordinate to establish an initial template's space, and then each subject image was resampled with respect to the initial template. The initial template's intensity was determined by computing the voxel-wise average of the training set. To generate the population average template, an iterative procedure was employed as follows [69], [104]:

- Each individual image was registered to the temporary template using affine and deformable Symmetric Normalization (SyN) transformation. For the first iteration, the temporary template is the initial template. After registration process, the temporary results consisted of (1) registered individual image, and (2) inverse transformation from the temporary template to individual image.
- The average of inverse transformations from the temporary template to each individual image was calculated. It was called new average transformation.
- The temporary template was updated by averaging the registered individual images.
- New average transformation was applied to the updated template.
- The process was iterated until the difference between the updated templates was minimized. Based on empirical study, four iterations are sufficient to generate an optimal ANTs template.

3.2.3. Evaluation before surgical planning

To determine how much of the variance in an individual's shape can be explained by the average population model, explained variations are calculated before applying the SSM for surgical planning. The analyze module in Shapeworks Studio provides the explained variations of the mean shapes, while PCA algorithm was applied to calculate the explained variations for the ANTs templates.

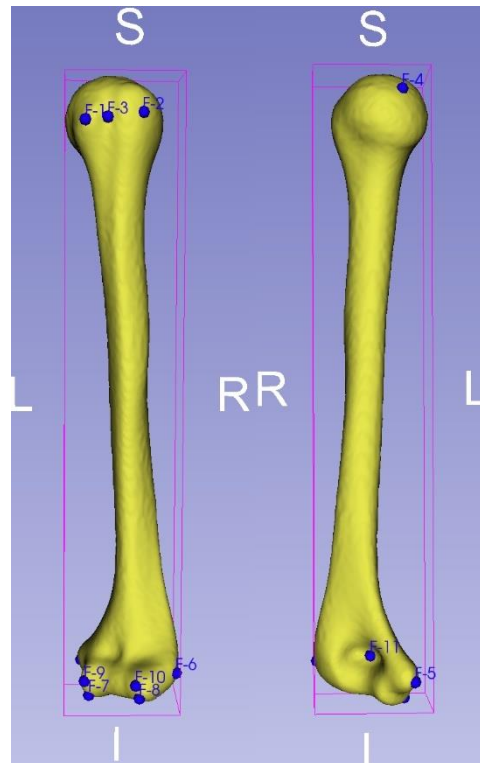


Figure 3-2: Eleven clinical landmarks were used for evaluation and validation.

First, as can be shown in Figure 3-2, an orthopedic surgeon determined sets of 11 anatomical landmarks on the ANTs templates. These anatomical landmarks are frequently utilized for clinical communication and as humerus surgery. To generate the correspondence landmark point clouds in each sub-dataset, these anatomical landmarks from the ANTs template (fixed image) were transformed to each subject image (moving image) in the training dataset by applying deformable registration. After the PCA process, the eigenvalue of each mode (principal model) was divided by the sum of all eigenvalues to determine the percentage of explained variation of each principal model [106]. Notice that the number of individuals minus one equals the number of models [97].

Distance models and distance histograms between the mean shapes and the ANTs templates were computed in 3D Slicer to evaluate the difference between two average population models. The segmentation module in 3D Slicer was used to reconstruct the ANTs template into a polydata, which then was registered to the mean shape using ICP registration. Next, the distance model was computed using the VTK Hausdorff.

3.2.4. Validation for surgical planning

The following steps were used to validate the context of surgical planning:

- Eleven anatomical landmarks at those clinical positions as shown in Figure 3-2 are manually determined by an expert on the SSM and each subject in the testing dataset. The annotations of each subject in the testing dataset worked as subject-specific ground truth.
- Eleven anatomical landmarks on the SSM were transferred to each subject in the testing dataset by applying the affine and deformable B-spline SyN. These transferred landmarks served as subject-predict landmarks.
- Determine the root mean square error (RMSE) between the subject-specific ground truth and the subject-predict landmarks.
- Apply paired t-test.

3.3. Results

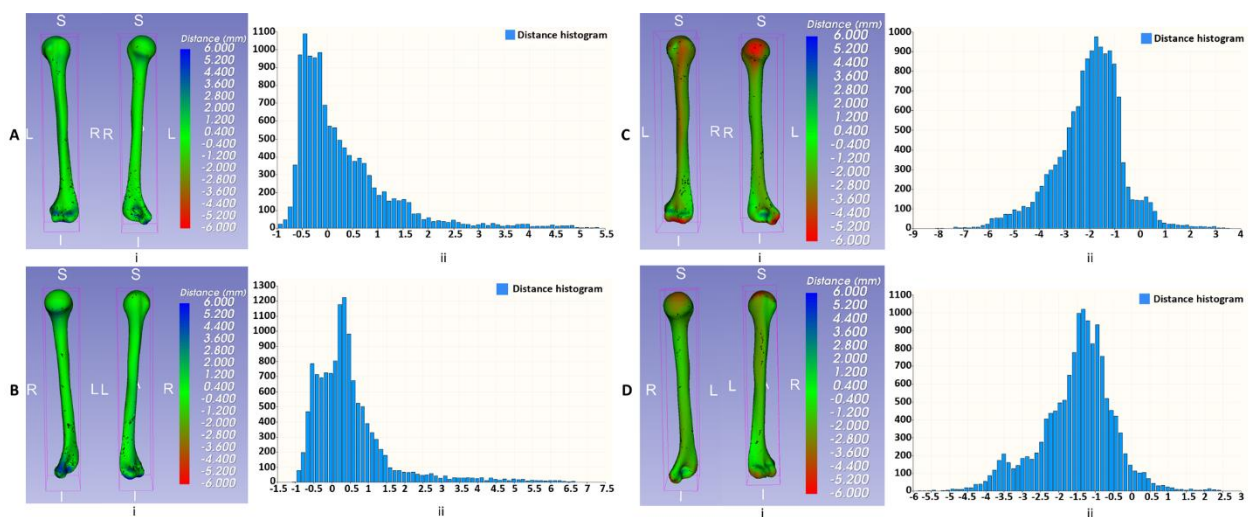


Figure 3-3: Distance models and correspondence histograms of distance values for each sub-dataset: A) Female-Left, B) Female-Right, C) Male-Left, D) Male-Right.

Figure 3-3 compares the shape and distance difference between the ANTs template and the Shapeworks mean shape. The distance range from minus 6 to 6 mm was encoded on an RGB color map, and a signed distance denoted that one model is inside the other.

First, the distance models and the corresponding histograms for female subjects were illustrated in Figure 3-3A and Figure 3-3B. The highest frequency bins of two histograms were mainly displayed in range from -0.5 mm to 1 mm, and the distance models were primary shown in green color. These results demonstrated that, in two cases of Female-Left and Female-Right, there are no significant differences in shape between the ANTs template and the Shapeworks mean shape.

Second, the distance values in the range from -2.5 mm to -1 mm and from -2 mm to 0.5 mm correspond to the maximum frequency bins of the histogram from Male-Left and Male-Right, respectively. A few red areas could be seen on the head on the Male-Left and Male-Right distance models, however not sufficient to effect on the global shape of the ANTs templates the Shapeworks mean shape.

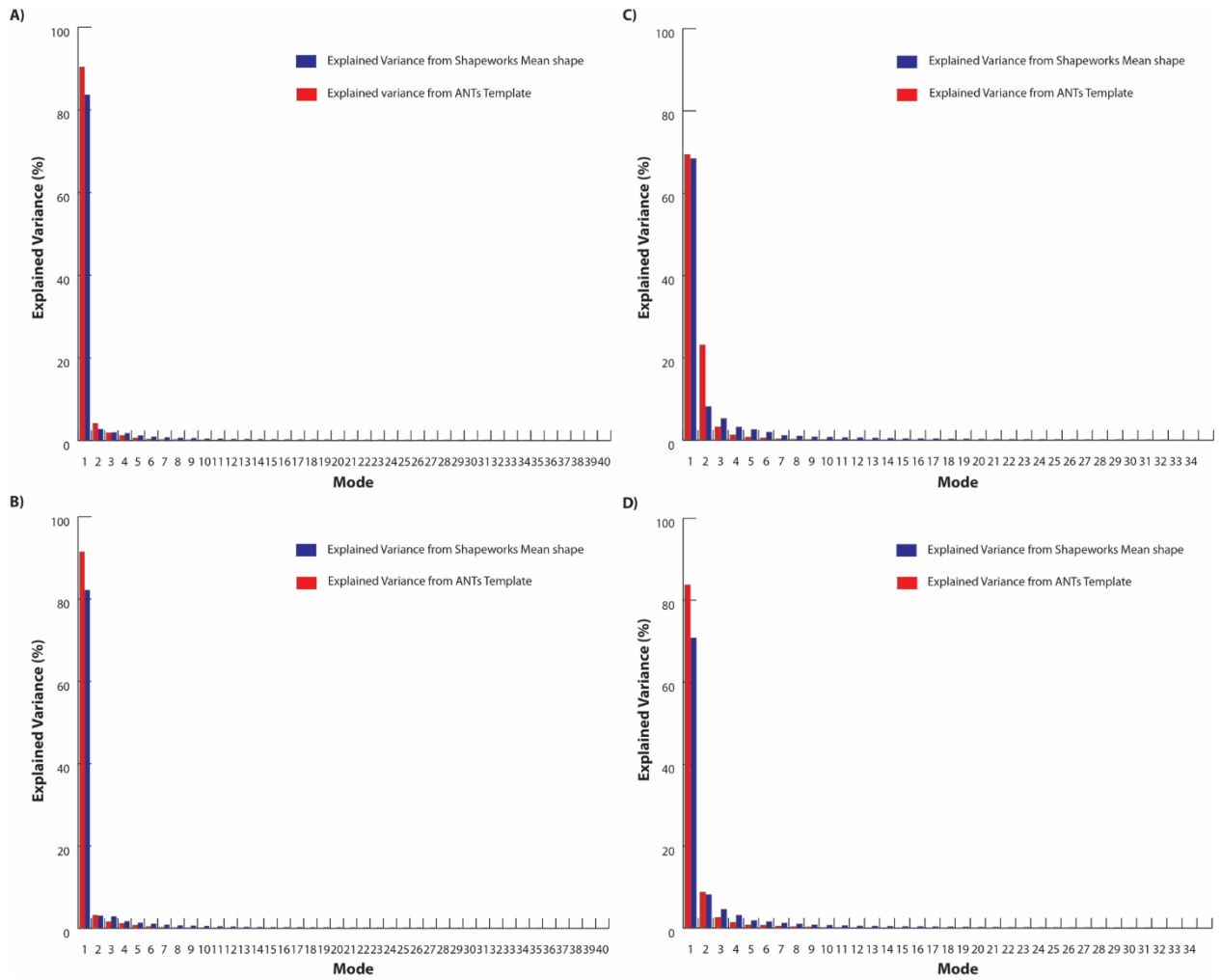
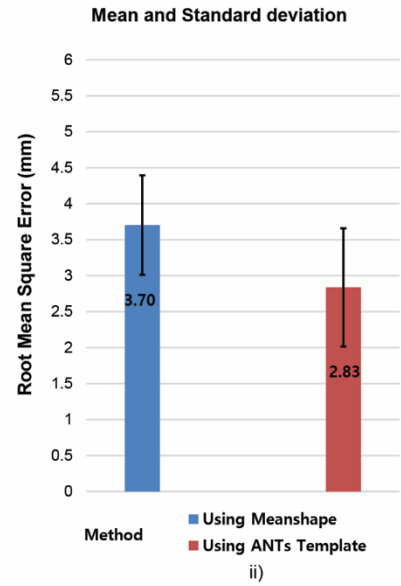
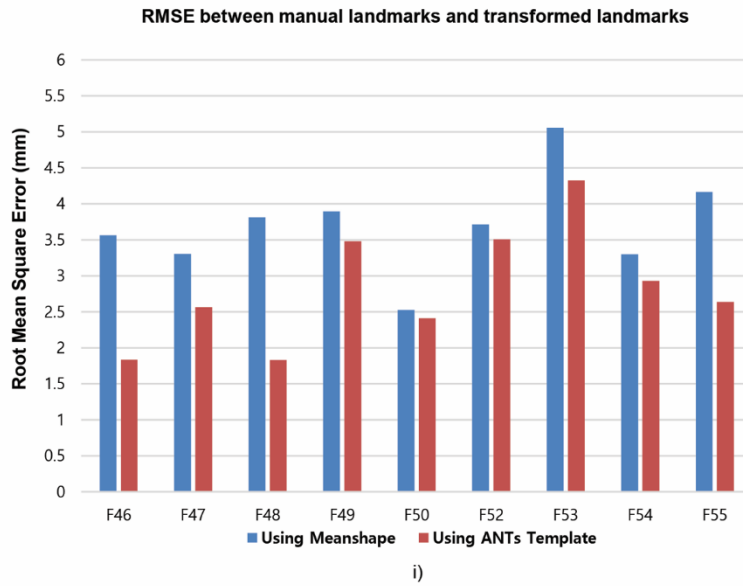


Figure 3-4: The explained variation of the SSM I each sub-dataset: a) Female-Left, b) Female-Right, c) Male-Left, d) Male-Right.

Figure 3-4 shows the explained variation for each sub-dataset when using Shapeworks and ANTs to model the SSM. Results presented that the first seven models of the average population model can represent 99% of the individual shape variance in all cases of the sub-dataset. However, compared to the mean shape generated by Shapeworks, the template built by ANTs can represent the variance of shape across individuals with a higher explained variation in four sub-datasets.

A) Female - Left



B) Female - Right

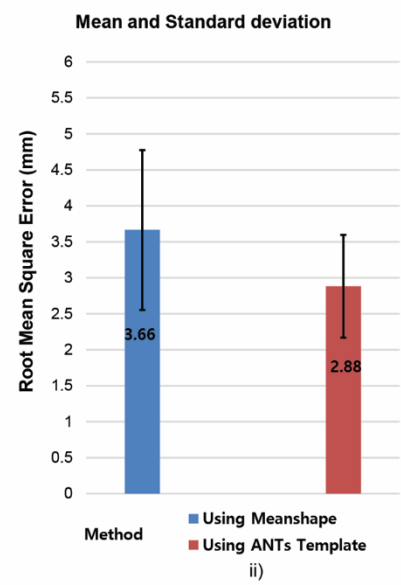
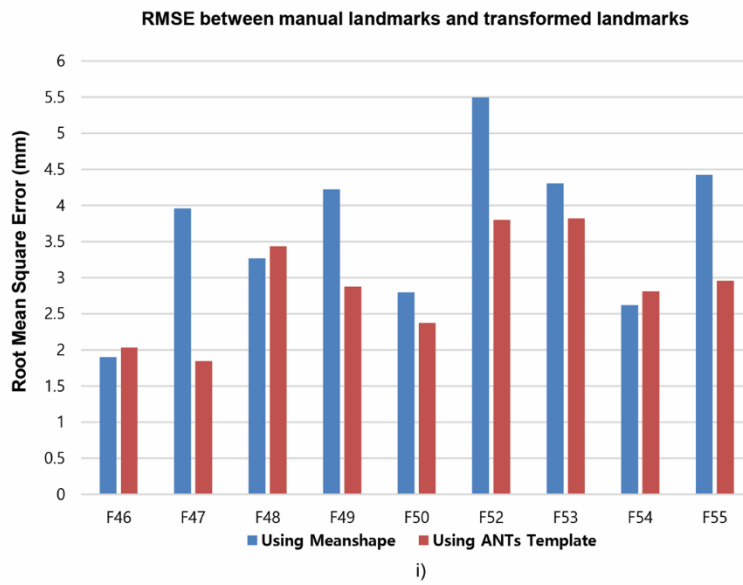
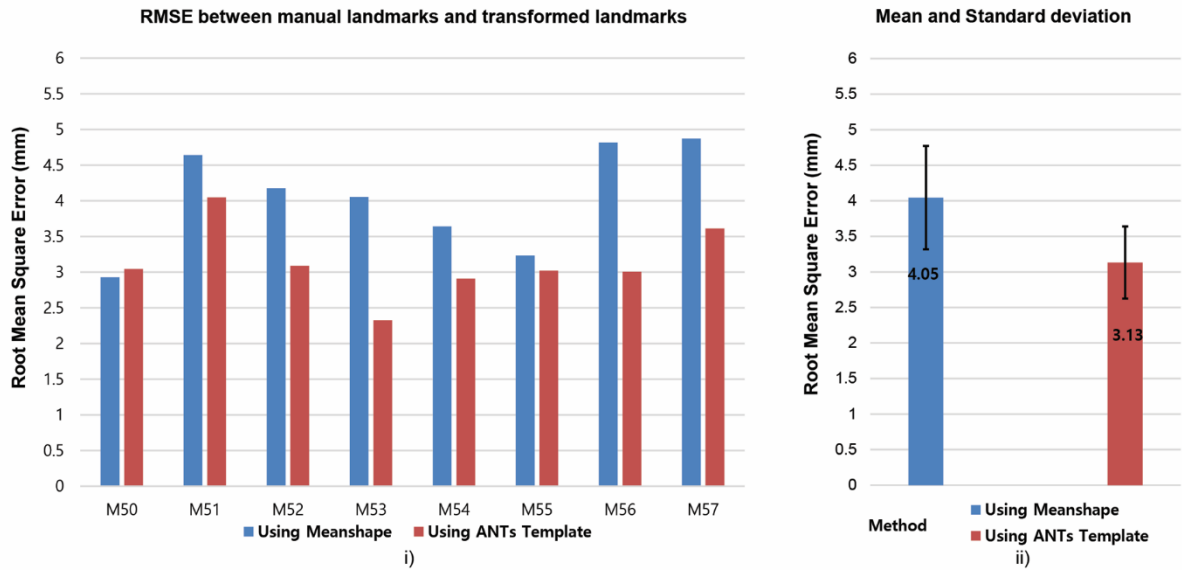


Figure 3-5: Humerus landmarks differences between the ground truth and prediction using SSMs in case of Female subjects: A) Left humerus (p -value < 0.05), B) Right humerus (p -value < 0.05).

A) Male - Left



B) Male - Right

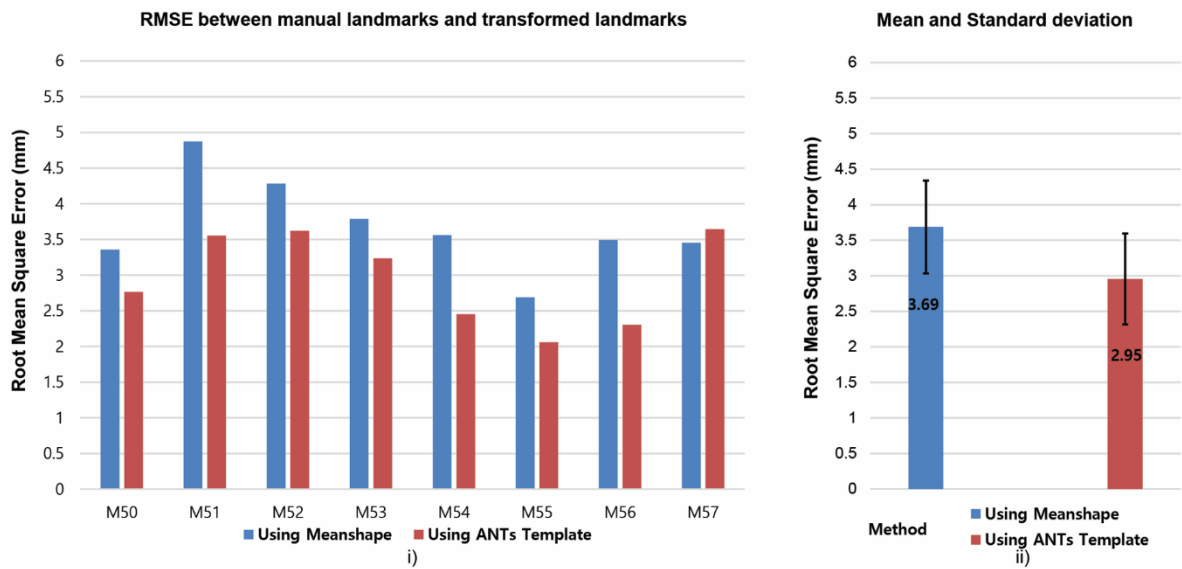


Figure 3-6: Humerus landmarks differences between the ground truth and prediction in case of Male subjects: A) Left humerus (p -value < 0.05), B) Right humerus (p -value < 0.05).

The differences in the position of the clinical landmarks between the ground truth and the predicted ones by the SSM were illustrated in Figure 3-5 and Figure 3-6, respectively. The minimum and maximum RMSE values are 2.83 mm and 3.13 mm in case of using ANTs, respectively, while the corresponding values in case of using Shapeworks are 3.66 mm and 4.05 mm, respectively.

3.4. Discussion and Conclusion

Surgical landmarking is essential for surgical planning in the context of clinical applications. For example, accurate implant insertion in surgical planning requires precise landmarking and accurate landmark specification is necessary for the development of bone

implanting in bone plates or total joint arthroplasty. This chapter developed an automatic surgical planning approach by using the average population model (or the SSM). The research entailed evaluating the shape and the explained variation of the average population model and verifying its ability to predict surgical landmark positions for new dataset that was not involved in process of building the average population model. ANTs and Shapeworks were applied to build the average population model, and the evaluation and validation results between ANTs template and Shapeworks mean shape were compared to report the improvement of using ANTs for surgical planning.

When determining surgical planning approach using the SSM, one of the fundamental factors that need to be considered is the shape. The results from Figure 3-3 and Figure 3-4 demonstrated that the shape of the ANTs template is better than the mean shape of Shapeworks with higher explained variation. The explained variation of an average population model is directly correlated with how well it can explain the variation in the involved individual shapes within the data.

Figure 3-5 and Figure 3-6 illustrate how the SSM generated by Shapeworks or ANTs could be utilized to estimate clinical landmark positions for new humerus dataset that was not included in the building of the SSM. Comparing the ANTs template to the Shapeworks mean shape, it was found that the ANTs template improved landmark position prediction with about 23%, 21%, 22%, and 20% in the cases of Female-Left, Female-Right, Male-Left, and Male-Right, respectively. Using ANTs templates demonstrated highly efficient results in automatically transferring surgical landmarks to ground truth points closely even though the templates were built from small-size datasets. These improvement results could be explained by the usage of the SyN algorithm in ANTs because this algorithm demonstrated the most consistently high accuracy registration across subjects in a comparison of 14 nonlinear deformation algorithms [72].

This chapter pointed out the ability of using an average population model for making automatically surgical planning for new patients who are not in the dataset used to generate the average population model. These abovementioned results could be considered in the development of an automated ANTs-based computer assisted surgical planning method.

To generate more reliable average population models, it should be expected that the proposed method would be expanded to broader surgical anatomy with larger datasets.

Chapter 4. Markerless registration approach using Dynamic Touchable Region model

4.1. Introduction

4.1.1. Related work

Registration is a crucial step in Image-guided Surgery (IGS) because it provides the corresponding transformation that aligns a physical object in the operating room (OR) with its view in the image coordinates [112], [113], [114], [115]. Medical imaging modalities such as MRI, CT, US, or the three-dimensional model generated from the object and displayed in an imaging tool such as 3D Slicer, could be used to describe the “view” definition. The conventional task in creating the transformation is to register between two pointsets from the image coordinates and the patient coordinates. Fiducial marker-based registration approach is commonly used for surgical assisting and navigation because this approach facilitates for the surgeons to determine corresponding paired points on the patient and imaging data.

Fiducial markers have been attached to the area surrounding the surgical lesion to aid in standard surgical guide techniques. The adhesive marker is one type of fiducial marker that is frequently used for surgical guiding. To ensure their stability while acquiring preoperative imaging data for registration process, they should be positioned on smooth surfaces rather than one with sharp protrusions, corners, or rough surfaces. Fiducial markers may move from their initial positions if they are not placed on a smooth surface because of the weak contact between the markers and the patient’s surface. The situation in a misalignment correspondence between the fiducial markers on the patient and those in the image data can lead to inaccuracies in registration. Inaccurate registration can result in registration errors, especially in neurosurgery where precision is crucial. Furthermore, the use of fiducial markers is prohibited for some operation procedures, such as orthopedic pedicle screw insertions and arthroplasty. Therefore, building and maintaining the corresponding paired points on the patient and the image coordinates using fiducial markers is challenging for such operations. A markerless registration approach is required in these cases, even though high accuracy may not be guaranteed.

The markerless registration process was used in several earlier research for IGS. The majority of methods have been suggested for orthopedic[115], [116], [117], cranial [118], and oral and maxillofacial surgery [119]. Using only the patient’s natural facial features, *Lee et al.* used an ICP method for cranial surgery, registering a 3D rebuilt facial surface measured by stereo vision with a facial surface generated from preoperative CT images [118]. They first recognized Harris corners in the left image before identifying corresponding feature points in the right image. After determining the correspondences, they reconstructed those feature points in three dimensions using the concepts of stereo vision. The study of *Lee et al.* showed the average target registration error (TRE) for five targets was 3.29 mm, which did not meet the requirement in the case of stereotactic frames, fiducial screws, or skin markers being replaced by the natural facial features. Due to the limitations of the stereo vision-based 3D reconstruction accuracy, the worst TRE was 5.13 mm. Furthermore, real-time IGS technique does not support the use of the Harris corner detector [120].

Using a similar method to *Lee et al.*, *Suenaga et al.* proposed real-time markerless registration for oral and maxillofacial surgery using a stereo camera [119]. From the CT data of participants, an integrative videography image and a 3D prototype model of the jaw were

generated. Subsequently, the 3D model's coordinates were registered with the contour obtained from the 3D scanner image in real space [119]. Although the results showed an improved average TRE than that of *Lee et al.*, the approach required a 3D surface reconstruction of the teeth as a prerequisite for registration. Furthermore, because of employing the stereo camera in both experiments of *Lee et al.* and *Suenaga et al.*, the registration error is dependent on the measurement precision of the stereo camera.

For orthopedic surgery, *Liu and Baena* and *Gao et al.* showed acceptable results by using a deep learning approach for markerless registration. *Gao et al.* designed an automatic fiducial-free 2D/3D registration pipeline based on a convolutional neural network (CNN) for intraoperative pose estimation for the femur, whereas *Liu and Baena* concentrated on building a region of interest (ROI) localization network with five convolutional layers to segment deep images in the knee surgical scenario [115], [116]. However, the complex *Gao et al.* pipeline requires landmark detection and consists of three stages: pelvis registration, femur registration, and device registration, whereas *Liu and Baena* captured a lot of the surrounding points with a depth camera so that the depth images contain noise and outliers because of the depth camera's low resolution. Moreover, another disadvantage of applying deep learning in the markerless registration field is that the complicated architecture of the depth image segmentation network requires strong computing power to speed up computation time.

Even though the earlier research, which benefited from developments in computer vision and medical image processing, presented encouraging results, they are not appropriate for use in IGS. The procedures for clinical applications registration are less precise and put patient safety at risk although these procedures could be conducted without interacting with users. Moreover, additional devices are required for registration and navigation. To facilitate navigation, at least two surgical tools should be tracked by using electromagnetic tracking system, depth camera, or optical tracking system (OTS) [121]. One of the most essential parts of the IGS system is the tracking system, which precisely determines the locations of the surgical tools and the anatomical areas they touch [122]. Therefore, the previously suggested approaches have been burdened with the operating room environment by requiring a second camera system to obtain the registration between the patient and image data. The limited space in the OR makes these approaches difficult to position the second camera close to the patient.

4.1.2. Contribution and acknowledgment

This chapter presents a markerless registration framework that improves registration accuracy without additional devices or procedures by using a dynamic touchable region model. The main goal is to identify the dynamic touchable region (DTR) which the surgeons can freely touch during a registration intraoperative procedure. The shape and size of the DTR might change based on how it is distributed. Next, a registration framework proposing the iterative closest dynamic touchable point (ICDTP) is described in this chapter. The ICDTP was developed based on the iterative closest touchable point (ICTP) approach, which was previously reported in a study of *Kim S and Kazanzides P* [123].

The method and results which present in this chapter were reported as parts of a journal article as follow:

- **Hang Phuong Nguyen, Taeho Kim, Sungmin Kim**, “Markerless registration approach using dynamic touchable region model”, *The International Journal of*

This work in this chapter was supported by the 2019 Research Fund of the University of Ulsan.

4.2. Materials and Methods

As illustrated in Figure 4-1, the proposed ICDTP method consists of three stages: (1) dynamic touchable region definition, (2) initial registration, and (3) fine registration. The dynamic touchable region was defined by Intrinsic Shape Signatures (ISS) keypoints, initial registration used paired-point registration (PPR), and the Iterative Closest Point (ICP) algorithm was applied for fine registration. Open 3D, an open-source toolkit for 3D data processing with Python [124], was used to establish the DTR, and both the initial registration and fine registration were implemented in Python.

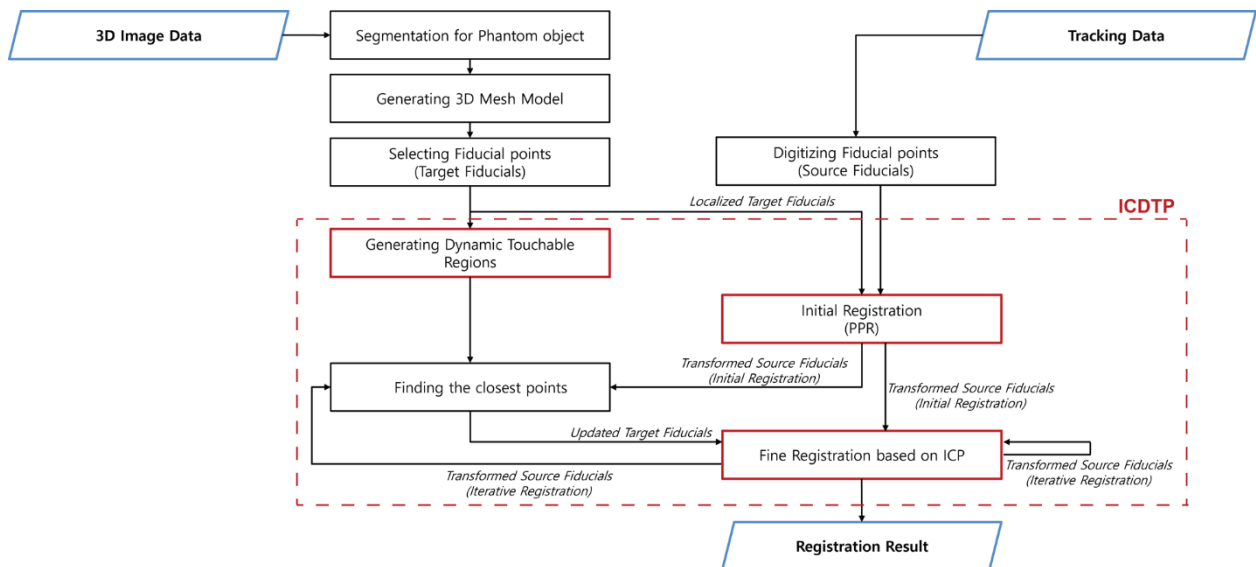


Figure 4-1: Markerless registration framework based on the ICDTP.

4.2.1. Definition of the Dynamic Touchable Region

Figure 4-2 presents the processes that were used to define the DTR. After importing the 3D mesh model generated from segmentation region, ISS keypoints were extracted to describe salient points or interesting points from the 3D model [125]. Even though there are some studies for detecting 3D keypoints, such as MeshDoG, Local Surface patches (LSP), Intrinsic Shape Signatures (ISS), KeyPoint Quality (KPQ), Heat Kernel Signature (HKS), and Laplace–Beltrami Scale-Space (LBSS), ISS was applied in the proposed framework due to its good performance and repeatability with a small and local 3D mesh model [126].

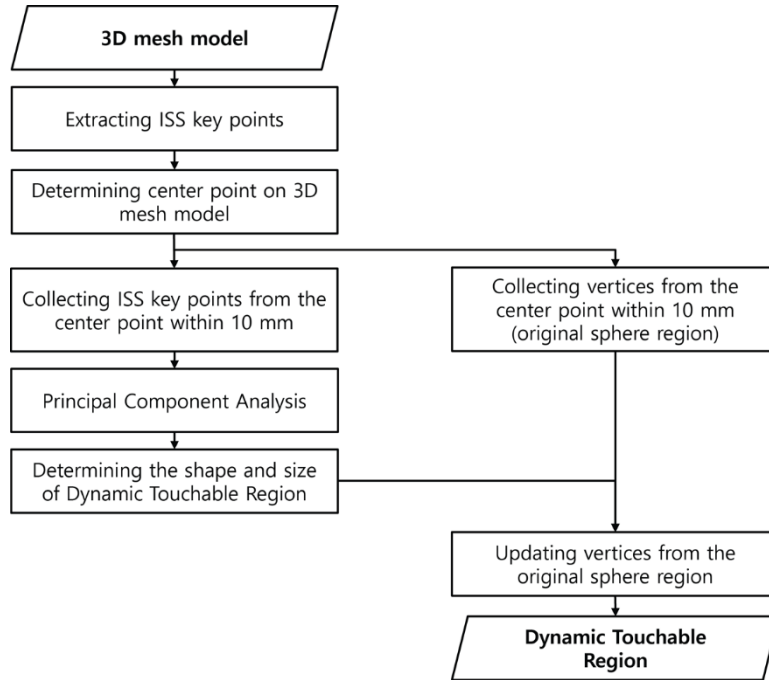


Figure 4-2: Procedure for the DTR definition. ISS is noted for Intrinsic Shape Signatures.

The DTR center point was then manually determined at the salient point on the surface of the 3D model. The position of the determined point was not always coinciding with one of the vertices on the 3D mesh model, therefore the nearest vertex with the determined point was then updated as the DTR center point. The k-d tree algorithm of the Open3D was used to find this nearest vertex.

The purpose of the DTR is representing the geometrical salient features of the surface while minimizing the searching space for the touchable region. The original searching space was a sphere which included all vertices within a given radius from the DTR center point (in this case, the radius was 10 mm). All ISS keypoints within 10 mm from the DTR center point were collected to describe the geometrical characteristics of the original sphere. Principal Component Analysis (PCA) was applied to identify the most significant direction of the dominant geometrical feature as determined by the ISS keypoints. Below equation 1, 2, and 3 were used to determine the shape and size of the DTR based on three eigenvalues of the PCA, where PC_i denoted the i^{th} principal component.

Equation 4 was used to calculate the length of each principal axis of the DTR. As shown in Figure 4-3, there are three cases to decide the shape and size of the DTR. The shape of the DTR was typically an ellipse with different lengths in the principal axes (as presented in Case 1, Figure 4-3b), or equal lengths in the median axis and the minor axis (as illustrated in Case 2, Figure 4-3c). The DTR shape was a sphere if each eigenvalue is equal, and the size of the DTR was reduced by halving the radius, as shown in case 3, Figure 4-3d. The final step in defining the DTR was to update the vertices belonging to the DTR following equation 5, where (x_0, y_0, z_0) is the coordinate of the center of the DTR, and a, b, and c are the principal semi-axes of the DTR.

$$\text{Variation for } PC_i = \frac{\text{Eigenvalue for } PC_i}{(\text{Number sample} - 1)} \quad (1)$$

$$\text{Variation percentage}_i = \frac{\text{Variation for } PC_i}{\text{Total variation}} \times 100\% \quad (2)$$

$$\lambda_i = \left(\frac{\text{Variation percentage}_i}{\text{Maximum variation percentage}} \right) \quad (3)$$

$$\text{Length of principal axis}_i = 2\lambda_i R \quad (4)$$

$$\frac{(x - x_0)^2}{(a)^2} + \frac{(y - y_0)^2}{(b)^2} + \frac{(z - z_0)^2}{(c)^2} \leq 1 \quad (5)$$

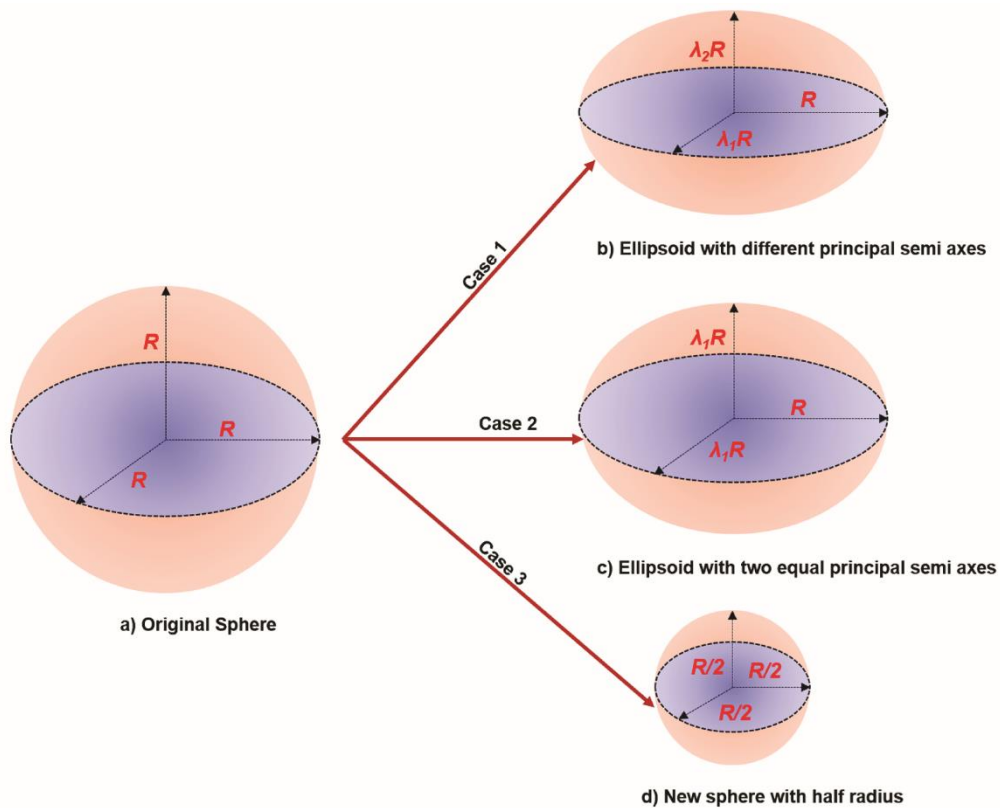


Figure 4-3: Change of shape from the original sphere (a) to the DTR (b-d), $0 < \lambda_i \leq 1$.

4.2.2. Registration using Dynamic Touchable Region

The approach of the ICDTP registration method is to apply the DTR for markerless registration. First, the digitized source fiducials (\mathbf{p}_s) collected from an optical tracking system were registered to target fiducials (\mathbf{p}_{LT}) localized on the 3D mesh model. The paired-point

algorithm was applied to the initial registration step. The initial transformation matrix was computed using equation 6. The transformed source fiducials then were computed by $\mathbf{p}_{TS} = T_I \mathbf{p}_S$, and applied to the fine registration.

$$T_I = \arg \min_{T_I} \sum_{i=1}^M \|\mathbf{p}_{LT_i} - T_I \mathbf{p}_{S_i}\|^2 \quad (6)$$

$$T_{ICDTP} = \arg \min_{T_{ICDTP}} \sum_{i=1}^M \|\mathbf{p}_{C_i} - T_{ICDTP} \mathbf{p}_{TS_i}\|^2 \quad (7)$$

Fine registration was inspired by the ICP registration method. The closest target point on each DTR \mathbf{p}_{C_i} was found by applying minimum Euclidean distance between the transformed source fiducial and the corresponding DTR. Equation 7 presented the calculation of ICDTP's transformation matrix, and the closest target points were updated after each iterative step. When the registration residual error converged, the fine registration stage would be finished.

4.2.3. Data analysis

To evaluate the accuracy of the proposed ICTP method, the registration residual error (RRE) and the TRE were calculated, and then those results were compared between the PPR method and the ICDTP method. The fiducial registration error (FRE) was the representation of the RRE in the PPR method. These errors were calculated by equation 8 and equation 9, respectively [127].

$$FRE = \sqrt{\frac{1}{M} \sum_{i=1}^M \|\mathbf{p}_{LT_i} - T_I \mathbf{p}_{S_i}\|^2} ; RRE = \sqrt{\frac{1}{M} \sum_{i=1}^M \|\mathbf{p}_{C_i} - T_{ICDTP} \mathbf{p}_{TS_i}\|^2} \quad (8)$$

$$TRE_{PPR} = \sqrt{\frac{1}{N} \sum_{j=1}^N \|\mathbf{p}_{Localized Target_j} - T_I \mathbf{p}_{Digitized Target_j}\|^2} ; \quad (9)$$

$$TRE_{ICDTP} = \sqrt{\frac{1}{N} \sum_{j=1}^N \|\mathbf{p}_{Localized Target_j} - T_{ICDTP} \mathbf{p}_{Digitized Target_j}\|^2} ,$$

4.3. Experiment

The experiment's main aims were to evaluate the DTR and to validate the accuracy of the ICDTP-based markerless registration framework. A geometrical phantom was used to evaluate the DTR. It was designed by 3D CAD software SolidWorks (Dassault Systems, Vélizy-Villacoublay, France) and manufactured with Evolve 128 material using a 3D printer (RSPro 800, UnionTech GmbH, Darmstadt, Germany). A 3D mesh model of this geometrical

phantom was built from the 3D CAD model using synthetic CT method. Three illustrations for the geometrical phantom were presented in Figure 4-4.

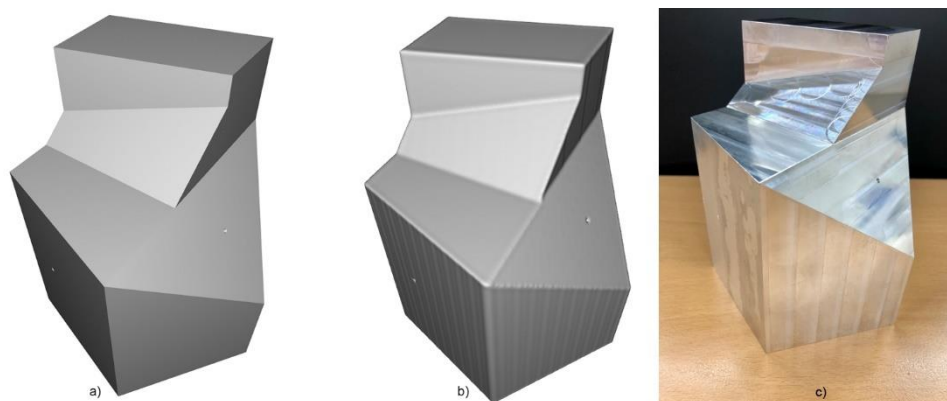


Figure 4-4: Geometrical model: a) Designed by 3D CAD software, b) Synthetic CT data simulation, c) Real phantom.



Figure 4-5: Skull phantom: a) 3D model built by laser scan data and a group of fiducials and targets, b) Real phantom and two notches serving as targets.

The ICDTP registration framework was validated using three different phantoms that mimicked human anatomies. They are skull phantom, spine phantom, and separable skull phantom, and were produced by Sawbones, a division of Pacific Research Laboratories, Inc., Vashon, Washington. To verify the proposed registration framework under different scenarios of 3D mesh model, three different approaches for building 3D mesh model were applied to the abovementioned phantom, each phantom corresponded to each approach. The skull mesh model presented in Figure 4-5a was built by laser scan data from the Sawbones digital product without any changes, the 3D spine mesh model was created by the synthetic CT method as represented in Figure 4-6a, whereas the real CT data of the separable skull model was used to construct the corresponding 3D mesh model as shown in Figure 4-7a.

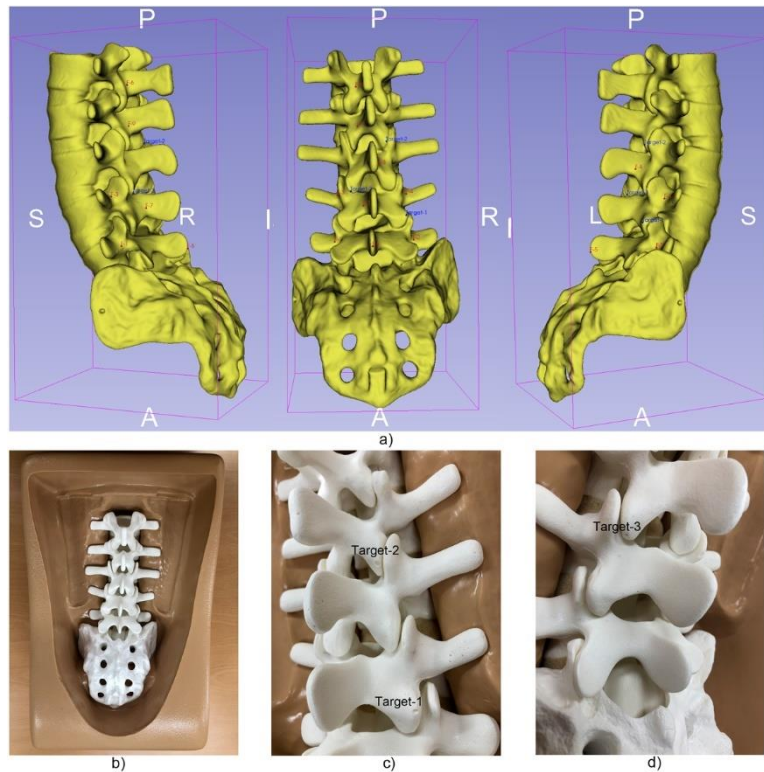


Figure 4-6: Spine phantom: a) 3D model built by simulated computer tomography data and a group of fiducials and targets, b) Real phantom built by a 3D printer and its holder, c and d) Three notches serving as targets.

For the DTR evaluation, each DTR on the geometrical phantom was determined following the process described in section 4.2.1 once the DTR's center point was identified on the edge of the geometrical phantom. Furthermore, the DTR evaluation was conducted on the skull, spine, and the separable skull mesh model.

No fiducial markers were placed on the phantoms because the purpose of this study was to improve registration accuracy in surgical scenarios that it was not suitable to apply the fiducial markers. Instead, target positions were established by localizing notches on the phantoms. There are two notches on the skull model as shown in Figure 4-5b, while there are three notches on the spine phantom as presented in Figure 4-6c,d.

Furthermore, to verify the proposed registration framework using DTR in the condition with deeper surgical lesions, three notches were embedded using non-metallic artificial free opaque CT marker (CT-23, Suremark company, AZ, USA) to serve as depth targets in the separable skull model, as presented in Figure 4-7c,d.

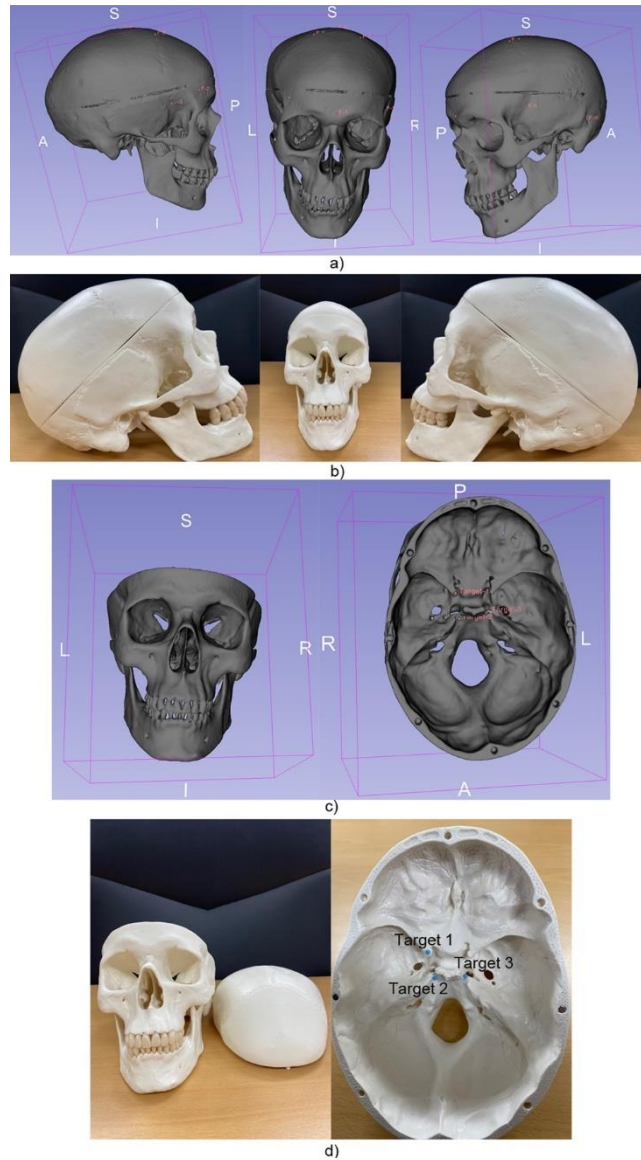


Figure 4-7: Separable skull phantom: a) 3D model built by real CT data and a group of fiducials, b) Real phantom, c) A group of three deep targets inside the separable skull model, d) Three deep targets inside the real phantom.

Two groups were set up for the registration experiments: the first group was single-user study, and the second group was multi-user study. Each participant in the multi-user study digitized the source fiducials once only, whereas every subject in the single-user study collected the source fiducials ten times. The participants were all non-surgeons or experts in surgical navigation field. The optical tracking system and the trackable digitizers were involved in the experiment as shown in Figure 4-8. The OTS provided the localization of the DTR center points and target notches in the physical space. The OTS used for the experiments is an optical tracking system SAKDI 1 (DigiTrack, Daegu, Korea) that can measure objects with distance from 500 mm to 1500 mm at 45 frames per second and has an accuracy of 0.2 mm RMS.

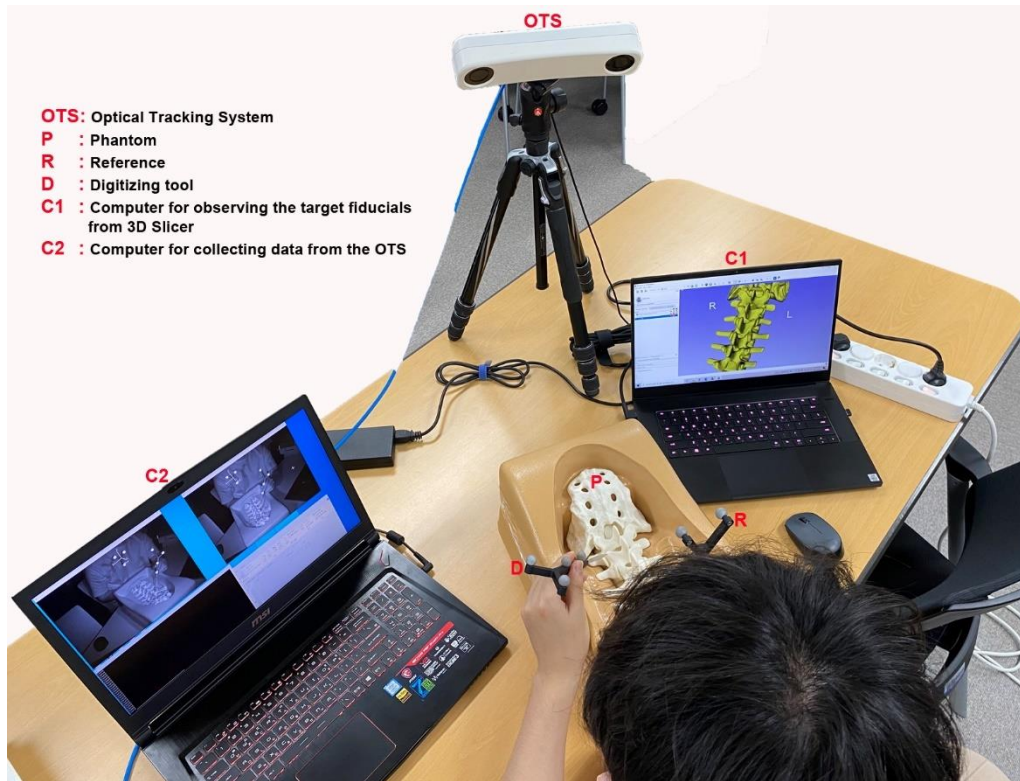


Figure 4-8: Setup for experiment.

Figure 4-8 showed the experimental configuration used in this chapter. The participant in the experiment used a digitizing tool to choose the source position on the real phantom while observing the corresponding fiducial displayed on the 3D mesh model via 3D Slicer. This procedure was then repeated nine times for nine different fiducials as well as two or three target notches depending on the phantom, as depicted in Figure 4-5, Figure 4-6, and Figure 4-7. The digitized location from the OTS was obtained by consecutively gathering one hundred position data points, and then averaged to reduce the OTS position data jittering.

4.4. Results

4.4.1. Evaluation of DTR

Three examples of principal component variation that made changing the shape and the size of the DTR were presented in Figure 4-9. Three DTRs were determined from three different center points that were placed on the sharp edges of the geometrical model. The percentages of principal components were computed and presented in the center of Figure 4-9 to provide clearly about the variation in each axis.

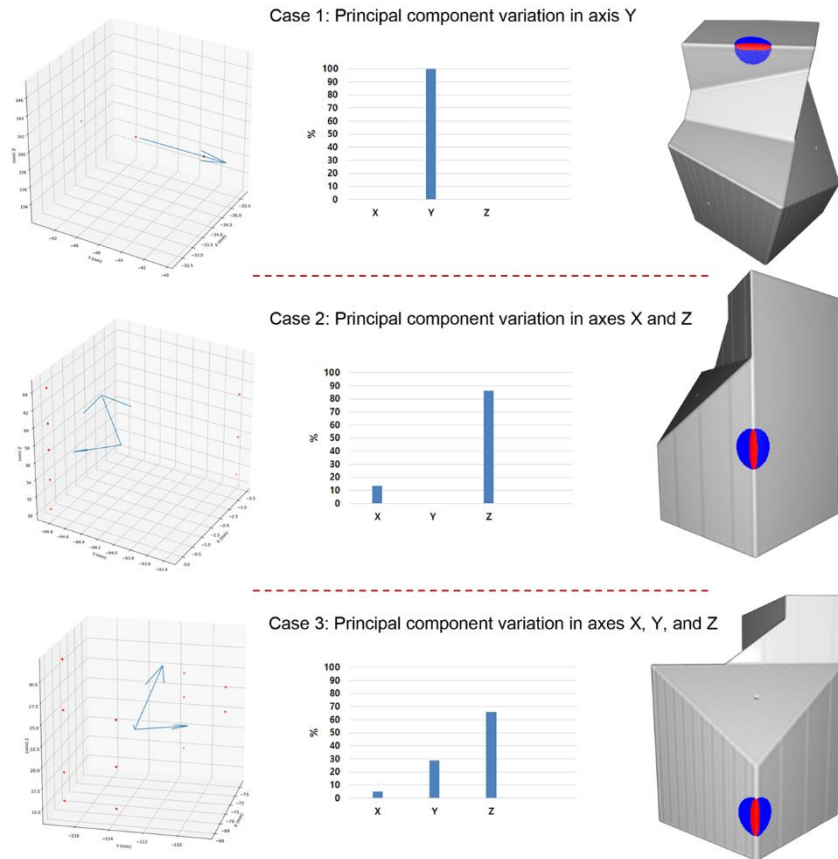


Figure 4-9: Three examples of principal component variation changing the DTR. The blue region presented the original sphere while the red region showed the dynamic touchable region.

Case 1 showed an example of 100% variation in direction Y, while two variations on the direction of X axis and Z axis were presented in Case 2 with 13.6% and 86.4% respectively, and the percentages of variation were 5.3, 28.7, and 66.0% respectively in Case 3. Although the principal component variation was different in each case, the DTRs kept expressing the dominant feature of region when compared to the original sphere, as shown as red regions in Figure 4-9.

Moreover, Figure 4-10 showed nine different DTRs for each 3D model of skull, spine, separable skull as results of validating the dynamic properties of the DTR. The positions of the DTRs were decided to determine the salient features of the regions of the DTRs.

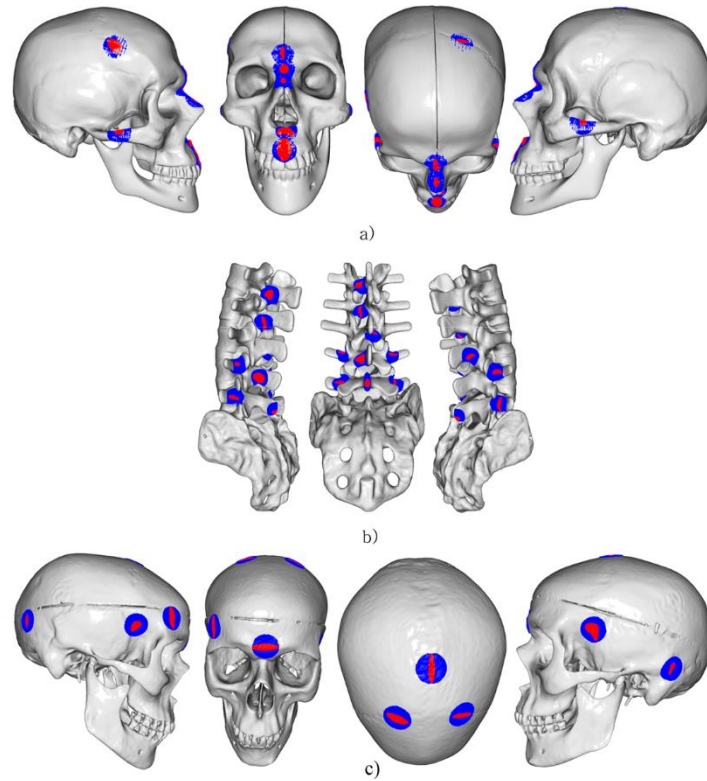


Figure 4-10: Dynamic touchable region used for markerless registration applied to a) skull model, b) spine model, and c) separable skull model.

4.4.2. ICDTP registration

The proposed registration method was compared with the conventional paired-point registration to evaluate the accuracy of the proposed framework as shown in Figure 4-1. The FRE of the PPR method and the RRE of the ICDTP registration method were measured, and the TRE for each registration method was computed.

Residual errors of the ICDTP registration method

The FRE and the RRE were depicted in Figure 4-11 and Figure 4-12 for the two experimental scenarios: the single-user study and the multi-user study utilizing the spine and the skull phantom, respectively.

Figure 4-11 illustrated that the mean of FRE was 1.98 mm and the mean of RRE was 0.36 mm in the experiment of single-user study applied to the skull model. Throughout all ten trials in the multi-user study, the accuracy of the RRE had improved over those of the FRE. Detailly, in the multi-user study, the mean of FRE was 3.25 mm while the mean of RRE was 0.57 mm. the RRE showed less variation across the participants (the worst case was 1.28 mm, the best case was 0.19 mm), whereas the FRE presents significant variation between participants (the worst case was 4.91 mm, the best case was 2.11 mm).

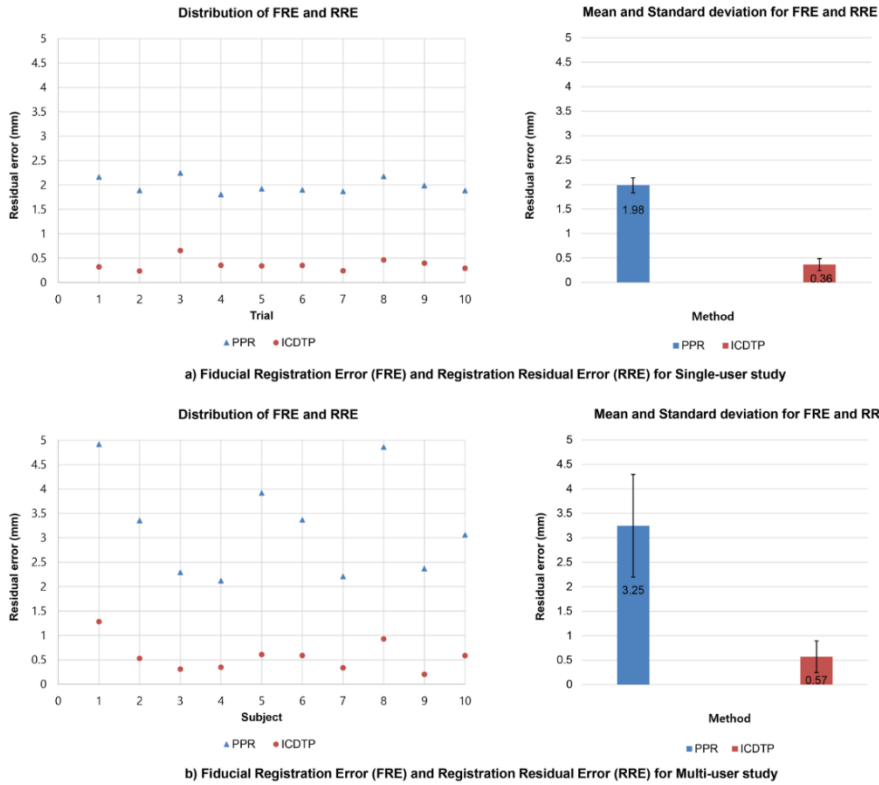


Figure 4-11: FRE and RRE for the skull phantom in a) single-user study and b) multi-user study.

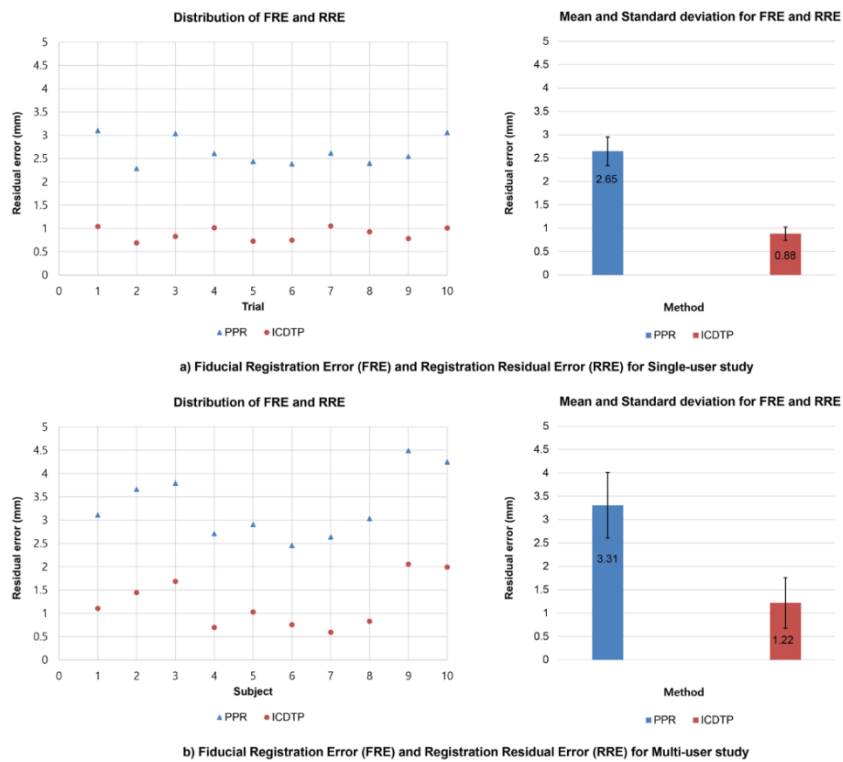


Figure 4-12: FRE and RRE for the spine phantom in a) single-user study and b) multi-user study.

Figure 4-12 showed that the trends of single-user study and the multi-user study in improving the residual error between applying the PPR and the ICDTP were consistent. For

every trial in the single-user study and every attendee in the multi-user study, the RRE value was less than the FRE value. Furthermore, the highest improvement was noted in the third trial of the single-user study (the RRE reduced 2.21 mm in comparison to the FRE) and the ninth participant in the multi-user study (the RRE value was 2.44 mm lower than the FRE).

Target registration errors of the ICDTP registration

The TREs from skull phantom experiments which were displayed in Figure 4-13 indicated the ICDTP method's higher precision than the PPR method. The proposed method improved the accuracy of the single-user study (Figure 4-13a) and the multi-user study (Figure 4-13b) by around 23% based on the average of the TREs. Detailly, ninety percent of ten trials conducted by the single user demonstrated the TRE results better than the PPR's. Only in the second trial of the single-user study where the TRE from the ICDTP was slightly higher than the PPR's (2.53 mm from ICDTP's compared to 2.27 mm from the PPR's). A similar conclusion occurred in the multi-user study. The results of the multi-user study indicated that the ICDTP method was more accurate than the PPR method in almost all trials. The only exception for the case of multiple participants was the sixth trial, where the TRE from ICDTP method (2.17 mm) slightly increased when compared to the PPR's (1.99 mm).

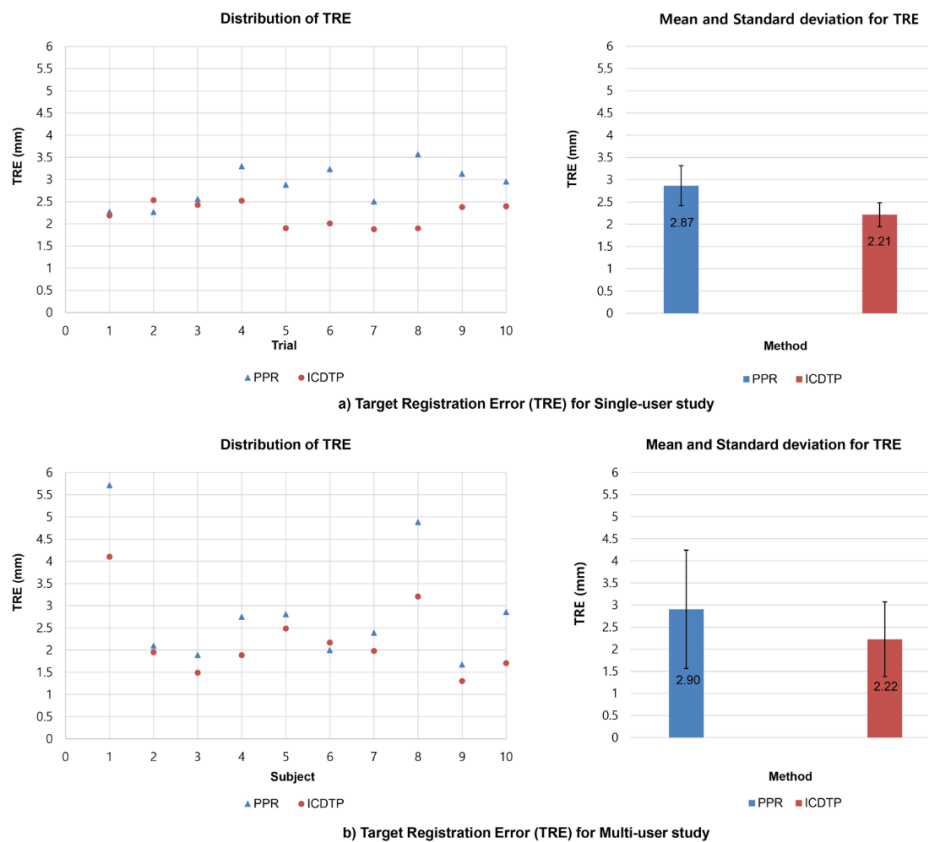


Figure 4-13: TREs with skull phantom for: a) single-user study (p -value < 0.05) and b) multi-user study (p -value < 0.05).

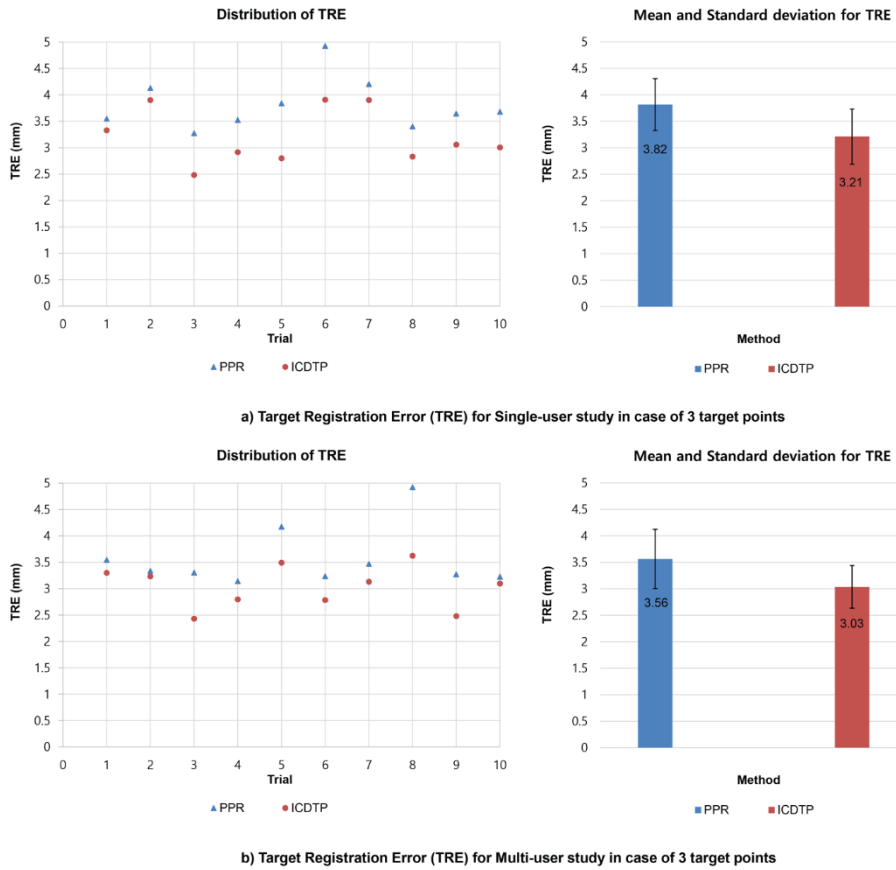


Figure 4-14: TREs with the spine phantom when tested with three targets in a) Single-user experiment (p -value < 0.001), b) Multi-user experiment (p -value < 0.05).

Three target points were used in the experiment on the spine phantom as illustrated in Figure 4-6c, d, and the TRE results were shown in Figure 4-14. The means of TREs using the PPR were 3.82 mm and 3.56 mm, whereas the means of TREs applying the ICDTP method were 3.21 mm and 3.03 mm, for the single-user study and the multi-user study, respectively. These results concluded that the accuracy of using the ICDTP method was higher than that of using the PPR.

The TREs from the experiment that used the ICDTP registration method to the separable skull model with three depth targets were shown in Figure 4-15. When compared to the PPR, all the TRE values from the ICDTP method in the single-user study and the multi-user study provided better accuracy. The TREs from the single-user and multi-user trial demonstrated improvements of 11.6% and 22.8%, respectively, when compared to the PPR.

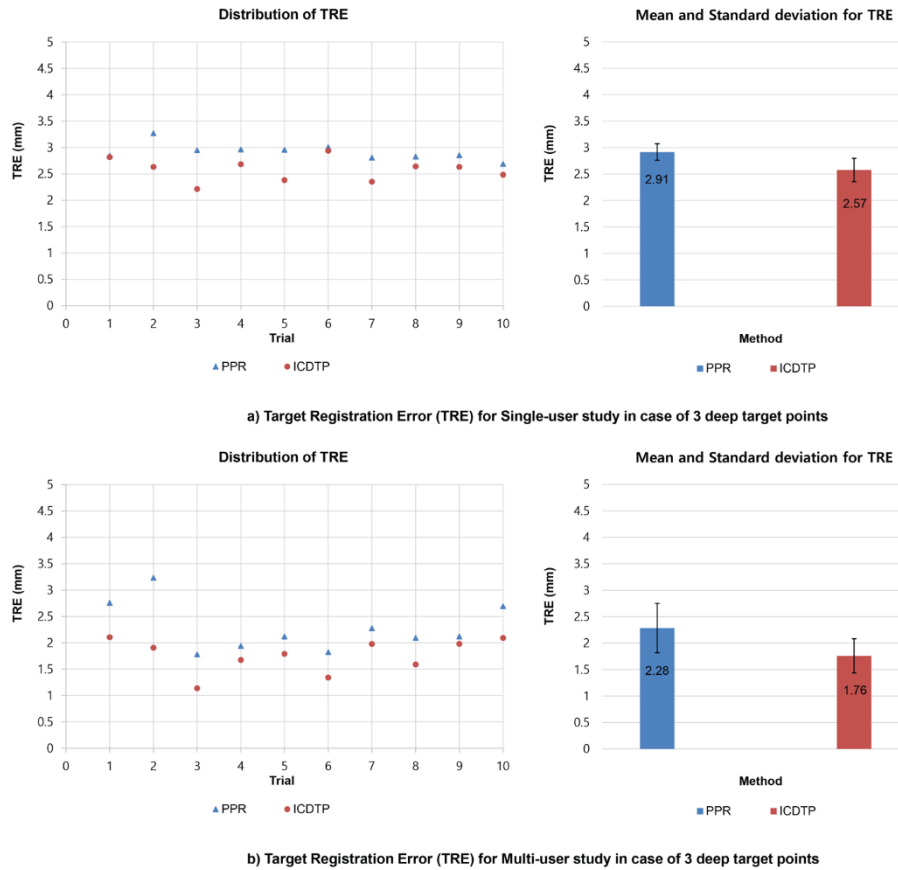


Figure 4-15: TREs of the separable skull phantom with three deep targets: a) Single-user experiment (p -value < 0.05), b) Multi-user experiment (p -value < 0.05).

4.5. Discussion

This chapter analyzed the proposed DTR and markerless registration based on ICDTP with phantom experiments. The discussion section first discussed the DTR and then the performance of the ICDTP method.

The process of defining the DTR was utilized using 3D mesh models. The original CAD model was used to generate the synthetic CT data for the geometrical phantom, as shown in Figure 4-4 a, b. The synthesized CT model had three times more vertex data than the CAD model, therefore it was sufficient for achieving good results for determining the DTR.

Figure 4-9 and Figure 4-10 demonstrated the robustness and adaptability of the proposed approach. Because of the effective ISS, any kind of 3D mesh model that was displayed as a 3D point cloud could be utilized to define the DTR. As mentioned in the section of Method, identifying ISS is one of the most crucial steps in the process of determining the DTR. This process worked directly on 3D point clouds and did not require surface meshing or triangulating the data points [125]. Furthermore, whereas the marker approach can not be used to the sharp edges, corners, and rough surfaces, the ISS can generate separate and highly discriminative representations for local/semi-local form patches, therefore allowing the DTR to be determined from a strong and rugged surface on the 3D mesh.

The ISS keypoints and PCA were used to define the DTR. PCA determined the direction and the size of the DTR by utilizing the distribution of the ISS keypoints, which characterized

the geometrical features and identified distinctive points at a certain surface around the fiducial area. According to the original ISS study [125], the intrinsic frame and the shape feature factor generated an independent representation of the local/semi-local 3D shape. Therefore, this contributed to the robustness and flexibility of the DTR.

Since the DTR's shape and size could affect how successfully the ICDTP registration worked, a simple single-user experiment was also conducted by comparing the TREs between the DTR-based method and a simple sphere-only approach (the original sphere). The spine phantom as presented in Figure 4-6 was used for the experiment, and the comparison results were displayed in Figure 4-16. The results from DTR-based method showed a considerable improvement in accuracy ($p < 0.05$) in contrast to the sphere-only approach, indicating that the DTR could provide meaningful improvement for markerless registration.

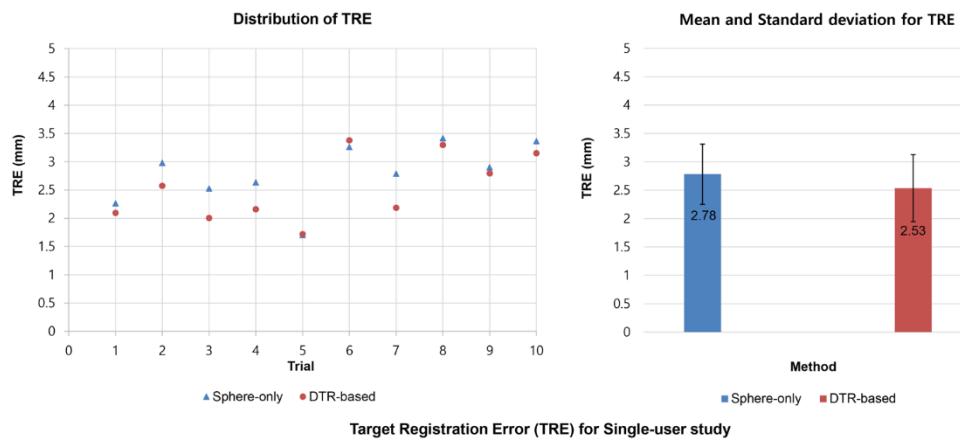


Figure 4-16: Comparison of TREs between sphere-only method and DTR-based method applying to the spine model in the single-user experiment (p -value = 0.01).

An experiment of applying a range of the DTR sizes (8, 10, 12, 14, and 15 mm in radius) to ICDTP registration in the spine phantom with single-user study was conducted, and the results were showed in Figure 4-17. The results presented that using DTR with 10mm radius provided the smallest value in the TRE when compared to other TREs computed from other DTR size. Therefore, it could be considered as the shape and size of the potential touchable region for surgeries of the spine and skull.

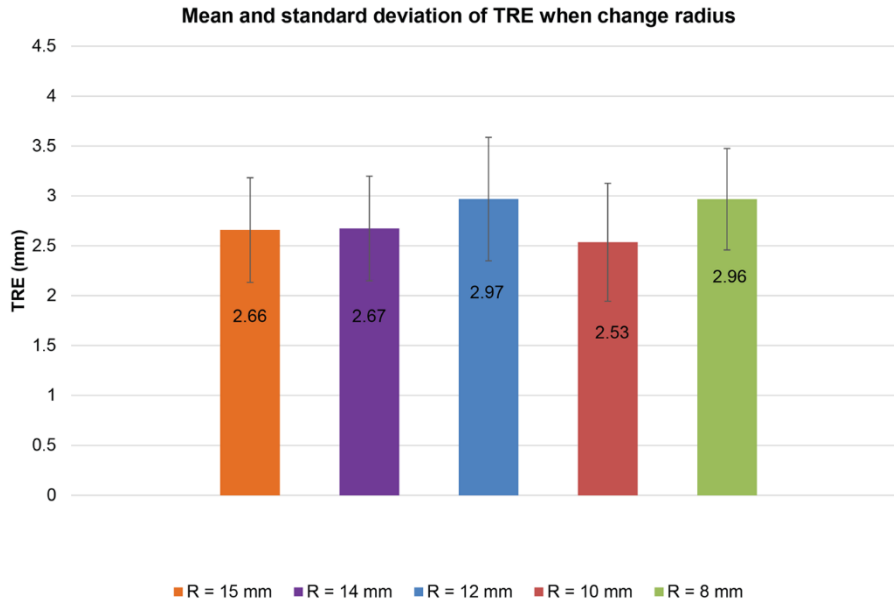


Figure 4-17: TREs at different radiuses of DTR applying for the spine model in the single-user experiment.

To evaluate the effectiveness of the proposed registration framework, the residual error and target registration error were calculated and reported in the section of results. The results demonstrated that when the DTR was employed in the markerless registration framework, the ICDTP performed more accurately than the conventional PPR.

Figure 4-11 and Figure 4-12 demonstrated the notable distinction between the residual errors of the ICDTP and PPR method. Since the intraoperative points could be paired to any position in the DTR rather than specific points following the PPR on the 3D mesh model, it is easy to explain why the RRE values were smaller than the corresponding FRE. It was necessary to make comparisons of TRE as presented in Figure 4-13, Figure 4-14, and Figure 4-15 because only improvements in RRE could not guarantee a better accuracy registration. These results showed that the ICDTP registration method significantly increased accuracy when compared to the conventional PPR registration. When utilizing a variety of anatomy-mimicking phantoms such as a skull phantom, a spine phantom, and a separable skull phantom, the ICDTP registration method consistently improved the TREs compared to the PPR method. This suggested that the ICDTP registration could be applied to a variety of surgical applications. Furthermore, the multi-user studies showed that the accuracy of the ICDTP approach was better than that of the PPR, indicating that the ICDTP approach is independent of users.

4.6. Conclusion

This chapter proposed a markerless registration approach ICDTP based on defining a dynamic touchable region DTR. The DTR allowed all feasible matches between the source fiducials collected using a digitizing tool and the targeted fiducials in the 3D coordinated of the 3D mesh model. There was no marker used during the point-collection process. To evaluate the accuracy of the proposed method, the results from ICDTP were compared to the results from the conventional PPR.

This chapter achieved two goals, the first one is that it established a comprehensive method for determining the DTR robustly, independently; second, it proposed and evaluated a

markerless registration framework using DTR. The registration results showed that the proposed ICDTP provided improved accuracy as compared to the conventional PPR.

Further research employing a more realistic phantom or cadaver would be conducted in the future to validate the proposed ICDTP method. Additionally, an ICDTP software module would be intended building on 3D Slicer and distributing it to other researchers and surgeons in the community of image-guided surgery.

Chapter 5. Conclusion

The work presented in this dissertation consisted of registration methods and automatic surgical planning method that were motivated by the thesis statement of “Research on automatic surgical planning and registration for Image-guided surgery”.

The dissertation developed throughout three major themes for image-guided surgery consisting of (1) proposing a framework for multimodal image registration between CT and MRI; (2) proposing a computer-assisted surgical planning method using statistical atlas and applying to the humerus surgery scenario; and (3) proposing a dynamic touchable region model applied to a framework for markerless registration in the intraoperative stage. These themes were described in chapter 2, chapter 3, and chapter 4, respectively.

Chapter 2 presented a framework for multimodal image registration in the preoperative process using a feature-based approach and image segmentation assistance was proposed to achieve complementary information from CT and MRI images. The surgical context was applied to the region of interest of the liver with 24 pairs of CT-MRI images. The framework proposed to use nnU-Net, an effective segmentation technique, to determine the region of interest (ROI) from both CT and MRI data. The significant spatial features of the ROI from both CT and MRI were then extracted by using CoLIAGes as independent descriptor images, and next descriptor images were registered by the deformable SyN algorithm of ANTs. The incorporation of segmentation into the registration pipeline ensured that the resulting transformation accurately reflected the anatomical correspondence, leading to better spatial alignment. This approach demonstrated significant improvements in registration accuracy and computing efficiency, establishing the path for more effective integration of multimodal imaging data in clinical diagnosis and treatment planning.

Chapter 3 reported a computer-assisted surgical planning method using novel forms of statistical shape models generated by Shapeworks and ANTs (Advanced Normalization Tools) and applied in a clinical scenario of humerus datasets to establish a framework for automatic surgical planning in the preoperative stage. This chapter developed an automatic surgical planning approach by using the statistical shape model (or average population model). The research entailed evaluating the shape and the explained variation of the average population model and verifying its ability to predict surgical landmark positions for new dataset that was not involved in process of building the average population model. ANTs and Shapeworks were applied to build the average population model, and the evaluation and validation results between ANTs template and Shapeworks mean shape were compared to report the improvement of using ANTs for surgical planning.

Chapter 4 provided a markerless registration framework using a dynamic touchable region model for intraoperative registration. The results were quantitatively evaluated in three different phantoms toward the clinical context. The registration results of the proposed method were also compared to the conventional paired-point registration. The dynamic touchable region model allowed all feasible matches between the source fiducials collected using a digitizing tool and the targeted fiducials in the 3D coordinated of the 3D mesh model. There was no marker used during the point-collection process. To evaluate the accuracy of the proposed method, the results from ICDTP were compared to the results from the conventional PPR. This chapter achieved two goals, the first one was that it established a comprehensive method for determining the DTR robustly, independently; second, it proposed and evaluated a

markerless registration framework using DTR. The registration results showed that the proposed ICDTP provided improved accuracy as compared to the conventional PPR.

References

- [1] K. Cleary and T. M. Peters, “Image-Guided Interventions: Technology Review and Clinical Applications,” *Annu. Rev. Biomed. Eng.*, vol. 12, no. 1, pp. 119–142, Jul. 2010, doi: 10.1146/annurev-bioeng-070909-105249.
- [2] T. M. Peters, J. Clark, B. Pike, M. Drangova, and A. Olivier, “Stereotactic surgical planning with magnetic resonance imaging, digital subtraction angiography and computed tomography,” *Appl Neurophysiol*, vol. 50, no. 1–6, pp. 33–38, 1987, doi: 10.1159/000100679.
- [3] T. M. Peters *et al.*, “Stereotactic neurosurgery planning on a personal-computer-based work station,” *J Digit Imaging*, vol. 2, no. 2, pp. 75–81, May 1989, doi: 10.1007/BF03168023.
- [4] C. E. Boone *et al.*, “MR-Guided Functional Neurosurgery: Laser Ablation and Deep Brain Stimulation,” *Topics in Magnetic Resonance Imaging*, vol. 27, no. 3, p. 171, Jun. 2018, doi: 10.1097/RMR.000000000000152.
- [5] A. Alqurashi *et al.*, “Accuracy of Pedicle Screw Placement Using Intraoperative CT-Guided Navigation and Conventional Fluoroscopy for Lumbar Spondylosis,” *Cureus*, vol. 13, no. 8, Aug. 2021, doi: 10.7759/cureus.17431.
- [6] E. Agricola, F. Meucci, F. Ancona, A. P. Sanz, and J. L. Zamorano, “Echocardiographic guidance in transcatheter structural cardiac interventions.” Accessed: Apr. 21, 2024. [Online]. Available: <https://eurointervention.pconline.com/article/echocardiographic-guidance-in-transcatheter-structural-cardiac-interventions>
- [7] J. A. Muñoz-Largacha, H. Batra, and B. Wei, “Navigational Bronchoscopy with Interventional Pulmonologists and Thoracic Surgeons,” *Innovations (Phila)*, vol. 16, no. 2, pp. 117–122, Mar. 2021, doi: 10.1177/1556984521997421.
- [8] A. Lawson McLean *et al.*, “Revitalizing neurosurgical frontiers: The EANS frontiers in neurosurgery committee’s strategic framework,” *Brain and Spine*, vol. 4, p. 102794, Jan. 2024, doi: 10.1016/j.bas.2024.102794.
- [9] M. Broggi *et al.*, “A Brief Explanation on Surgical Approaches for Treatment of Different Brain Tumors,” *Adv Exp Med Biol*, vol. 1405, pp. 689–714, 2023, doi: 10.1007/978-3-031-23705-8_27.
- [10] F. Winter *et al.*, “Current state of the art of traditional and minimal invasive epilepsy surgery approaches,” *Brain and Spine*, vol. 4, p. 102755, Jan. 2024, doi: 10.1016/j.bas.2024.102755.
- [11] M. Mahvash *et al.*, “FLAIR-/T1-/T2-co-registration for image-guided diagnostic and resective epilepsy surgery,” *Neurosurgery*, vol. 62 Suppl 2, pp. 482–488, Feb. 2008, doi: 10.1227/01.neu.0000316251.47028.f6.

- [12] X. Fan, Q. Zhu, P. Tu, L. Joskowicz, and X. Chen, “A review of advances in image-guided orthopedic surgery,” *Phys Med Biol*, vol. 68, no. 2, Jan. 2023, doi: 10.1088/1361-6560/acaae9.
- [13] C. A. Linte *et al.*, “Accuracy Considerations in Image-guided Cardiac Interventions: Experience and Lessons Learned,” *Int J Comput Assist Radiol Surg*, vol. 7, no. 1, pp. 13–25, Jan. 2012, doi: 10.1007/s11548-011-0621-1.
- [14] C. A. Linte, A. Wiles, J. Moore, C. Wedlake, and T. M. Peters, “Virtual reality-enhanced ultrasound guidance for atrial ablation: in vitro epicardial study,” *Med Image Comput Comput Assist Interv*, vol. 11, no. Pt 2, pp. 644–651, 2008, doi: 10.1007/978-3-540-85990-1_77.
- [15] M. E. Rettmann, D. R. Holmes, B. M. Cameron, and R. A. Robb, “An event-driven distributed processing architecture for image-guided cardiac ablation therapy,” *Comput Methods Programs Biomed*, vol. 95, no. 2, pp. 95–104, Aug. 2009, doi: 10.1016/j.cmpb.2009.01.009.
- [16] M. E. Rettmann *et al.*, “An integrated system for real-time image guided cardiac catheter ablation,” *Stud Health Technol Inform*, vol. 119, pp. 455–460, 2006.
- [17] M. M. Arnolli, M. Buijze, M. Franken, K. P. de Jong, D. M. Brouwer, and I. A. M. J. Broeders, “System for CT-guided needle placement in the thorax and abdomen: A design for clinical acceptability, applicability and usability,” *Robotics Computer Surgery*, vol. 14, no. 1, p. e1877, Feb. 2018, doi: 10.1002/rcs.1877.
- [18] S. Pieper, M. Halle, and R. Kikinis, “3D Slicer,” in *2004 2nd IEEE International Symposium on Biomedical Imaging: Macro to Nano (IEEE Cat No. 04EX821)*, Arlington, VA, USA: IEEE, 2004, pp. 632–635. doi: 10.1109/ISBI.2004.1398617.
- [19] D. L. Hill, P. G. Batchelor, M. Holden, and D. J. Hawkes, “Medical image registration,” *Phys Med Biol*, vol. 46, no. 3, pp. R1-45, Mar. 2001, doi: 10.1088/0031-9155/46/3/201.
- [20] Z. M. C. Baum, Y. Hu, and D. C. Barratt, “Real-time multimodal image registration with partial intraoperative point-set data,” *Medical Image Analysis*, vol. 74, p. 102231, Dec. 2021, doi: 10.1016/j.media.2021.102231.
- [21] B. Rister, M. A. Horowitz, and D. L. Rubin, “Volumetric Image Registration From Invariant Keypoints,” *IEEE Trans. on Image Process.*, vol. 26, no. 10, pp. 4900–4910, Oct. 2017, doi: 10.1109/TIP.2017.2722689.
- [22] Y. Hu *et al.*, “Weakly-supervised convolutional neural networks for multimodal image registration,” *Medical Image Analysis*, vol. 49, pp. 1–13, Oct. 2018, doi: 10.1016/j.media.2018.07.002.
- [23] C. M. C. Tempany *et al.*, “Multimodal imaging for improved diagnosis and treatment of cancers,” *Cancer*, vol. 121, no. 6, pp. 817–827, Mar. 2015, doi: 10.1002/cncr.29012.
- [24] H. Elhawary *et al.*, “Multimodality Non-rigid Image Registration for Planning, Targeting and Monitoring During CT-Guided Percutaneous Liver Tumor Cryoablation,” *Academic Radiology*, vol. 17, no. 11, pp. 1334–1344, Nov. 2010, doi: 10.1016/j.acra.2010.06.004.

- [25] V. Fortunati *et al.*, “Feasibility of Multimodal Deformable Registration for Head and Neck Tumor Treatment Planning,” *International Journal of Radiation Oncology*Biophysics*, vol. 90, no. 1, pp. 85–93, Sep. 2014, doi: 10.1016/j.ijrobp.2014.05.027.
- [26] E. M. McKenzie, A. Santhanam, D. Ruan, D. O’Connor, M. Cao, and K. Sheng, “Multimodality image registration in the head-and-neck using a deep learning-derived synthetic CT as a bridge,” *Medical Physics*, vol. 47, no. 3, pp. 1094–1104, Mar. 2020, doi: 10.1002/mp.13976.
- [27] X. Tang *et al.*, “Segmentation-guided multi-modal registration of liver images for dose estimation in SIRT,” *EJNMMI Phys*, vol. 9, no. 1, p. 3, Dec. 2022, doi: 10.1186/s40658-022-00432-8.
- [28] E. Jafarholi Rangraz, W. Coudyzer, G. Maleux, K. Baete, C. M. Deroose, and J. Nuyts, “Multi-modal image analysis for semi-automatic segmentation of the total liver and liver arterial perfusion territories for radioembolization,” *EJNMMI Res*, vol. 9, no. 1, p. 19, Dec. 2019, doi: 10.1186/s13550-019-0485-x.
- [29] X. Cao, J. Yang, Y. Gao, Y. Guo, G. Wu, and D. Shen, “Dual-core steered non-rigid registration for multi-modal images via bi-directional image synthesis,” *Medical Image Analysis*, vol. 41, pp. 18–31, Oct. 2017, doi: 10.1016/j.media.2017.05.004.
- [30] X. Cao, Y. Gao, J. Yang, G. Wu, and D. Shen, “Learning-Based Multimodal Image Registration for Prostate Cancer Radiation Therapy,” in *Medical Image Computing and Computer-Assisted Intervention - MICCAI 2016*, vol. 9902, in Lecture Notes in Computer Science, vol. 9902. , 2016, pp. 1–9. doi: 10.1007/978-3-319-46726-9_1.
- [31] X. Cao, J. Yang, Y. Gao, Q. Wang, and D. Shen, “Region-Adaptive Deformable Registration of CT/MRI Pelvic Images via Learning-Based Image Synthesis,” *IEEE Trans. on Image Process.*, vol. 27, no. 7, pp. 3500–3512, Jul. 2018, doi: 10.1109/TIP.2018.2820424.
- [32] M. P. Heinrich *et al.*, “MIND: Modality independent neighbourhood descriptor for multi-modal deformable registration,” *Medical Image Analysis*, vol. 16, no. 7, pp. 1423–1435, Oct. 2012, doi: 10.1016/j.media.2012.05.008.
- [33] S. Roy, A. Carass, A. Jog, J. L. Prince, and J. Lee, “MR to CT registration of brains using image synthesis,” presented at the SPIE Medical Imaging, S. Ourselin and M. A. Styner, Eds., San Diego, California, USA, Mar. 2014, p. 903419. doi: 10.1117/12.2043954.
- [34] J. Lee, A. Carass, A. Jog, C. Zhao, and J. L. Prince, “Multi-atlas-based CT synthesis from conventional MRI with patch-based refinement for MRI-based radiotherapy planning,” presented at the SPIE Medical Imaging, M. A. Styner and E. D. Angelini, Eds., Orlando, Florida, United States, Feb. 2017, p. 101331I. doi: 10.1117/12.2254571.
- [35] E. P. Pappas *et al.*, “MRI-Related Geometric Distortions in Stereotactic Radiotherapy Treatment Planning: Evaluation and Dosimetric Impact,” *Technol Cancer Res Treat*, vol. 16, no. 6, pp. 1120–1129, Dec. 2017, doi: 10.1177/1533034617735454.

- [36] P. Jezzard and R. S. Balaban, “Correction for geometric distortion in echo planar images from B0 field variations,” *Magn Reson Med*, vol. 34, no. 1, pp. 65–73, Jul. 1995, doi: 10.1002/mrm.1910340111.
- [37] A. Janke, H. Zhao, G. J. Cowin, G. J. Galloway, and D. M. Doddrell, “Use of spherical harmonic deconvolution methods to compensate for nonlinear gradient effects on MRI images,” *Magn Reson Med*, vol. 52, no. 1, pp. 115–122, Jul. 2004, doi: 10.1002/mrm.20122.
- [38] D. Rueckert, L. I. Sonoda, C. Hayes, D. L. G. Hill, M. O. Leach, and D. J. Hawkes, “Nonrigid registration using free-form deformations: application to breast MR images,” *IEEE Trans. Med. Imaging*, vol. 18, no. 8, pp. 712–721, Aug. 1999, doi: 10.1109/42.796284.
- [39] S. J. Doran, L. Charles-Edwards, S. A. Reinsberg, and M. O. Leach, “A complete distortion correction for MR images: I. Gradient warp correction,” *Phys Med Biol*, vol. 50, no. 7, pp. 1343–1361, Apr. 2005, doi: 10.1088/0031-9155/50/7/001.
- [40] W. M. Wells, P. Viola, H. Atsumi, S. Nakajima, and R. Kikinis, “Multi-modal volume registration by maximization of mutual information,” *Med Image Anal*, vol. 1, no. 1, pp. 35–51, Mar. 1996, doi: 10.1016/s1361-8415(01)80004-9.
- [41] J. P. W. Pluim, J. B. A. Maintz, and M. A. Viergever, “Mutual-information-based registration of medical images: a survey,” *IEEE Trans. Med. Imaging*, vol. 22, no. 8, pp. 986–1004, Aug. 2003, doi: 10.1109/TMI.2003.815867.
- [42] J. Woo, M. Stone, and J. L. Prince, “Multimodal Registration via Mutual Information Incorporating Geometric and Spatial Context,” *IEEE Trans. on Image Process.*, vol. 24, no. 2, pp. 757–769, Feb. 2015, doi: 10.1109/TIP.2014.2387019.
- [43] T. Huynh *et al.*, “Estimating CT Image From MRI Data Using Structured Random Forest and Auto-Context Model,” *IEEE Trans. Med. Imaging*, vol. 35, no. 1, pp. 174–183, Jan. 2016, doi: 10.1109/TMI.2015.2461533.
- [44] A. Johansson, M. Karlsson, and T. Nyholm, “CT substitute derived from MRI sequences with ultrashort echo time,” *Med Phys*, vol. 38, no. 5, pp. 2708–2714, May 2011, doi: 10.1118/1.3578928.
- [45] S. Roy, W.-T. Wang, A. Carass, J. L. Prince, J. A. Butman, and D. L. Pham, “PET attenuation correction using synthetic CT from ultrashort echo-time MR imaging,” *J Nucl Med*, vol. 55, no. 12, pp. 2071–2077, Dec. 2014, doi: 10.2967/jnumed.114.143958.
- [46] D. Nie, X. Cao, Y. Gao, L. Wang, and D. Shen, “Estimating CT Image from MRI Data Using 3D Fully Convolutional Networks,” *Deep Learn Data Label Med Appl (2016)*, vol. 2016, pp. 170–178, 2016, doi: 10.1007/978-3-319-46976-8_18.
- [47] G. Wu, F. Qi, and D. Shen, “Learning-based deformable registration of MR brain images,” *IEEE Transactions on Medical Imaging*, vol. 25, no. 9, pp. 1145–1157, Sep. 2006, doi: 10.1109/TMI.2006.879320.

- [48] T. Brox and J. Malik, “Large Displacement Optical Flow: Descriptor Matching in Variational Motion Estimation,” *IEEE Transactions on Pattern Analysis and Machine Intelligence*, vol. 33, no. 3, pp. 500–513, Mar. 2011, doi: 10.1109/TPAMI.2010.143.
- [49] Y. Ou, A. Sotiras, N. Paragios, and C. Davatzikos, “DRAMMS: Deformable Registration via Attribute Matching and Mutual-Saliency Weighting,” *Med Image Anal*, vol. 15, no. 4, pp. 622–639, Aug. 2011, doi: 10.1016/j.media.2010.07.002.
- [50] D. G. Lowe, “Object recognition from local scale-invariant features,” in *Proceedings of the Seventh IEEE International Conference on Computer Vision*, Sep. 1999, pp. 1150–1157 vol.2. doi: 10.1109/ICCV.1999.790410.
- [51] K. Mikolajczyk and C. Schmid, “A performance evaluation of local descriptors,” *IEEE Transactions on Pattern Analysis and Machine Intelligence*, vol. 27, no. 10, pp. 1615–1630, Oct. 2005, doi: 10.1109/TPAMI.2005.188.
- [52] O. Ronneberger, P. Fischer, and T. Brox, “U-Net: Convolutional Networks for Biomedical Image Segmentation.” arXiv, May 18, 2015. Accessed: May 23, 2024. [Online]. Available: <http://arxiv.org/abs/1505.04597>
- [53] S. Tavakoli, A. Ghaffari, Z. M. Kouzehkanan, and R. Hosseini, “New segmentation and feature extraction algorithm for classification of white blood cells in peripheral smear images,” *Sci Rep*, vol. 11, no. 1, p. 19428, Sep. 2021, doi: 10.1038/s41598-021-98599-0.
- [54] J. Ashburner and K. Friston, “Multimodal image coregistration and partitioning—a unified framework,” *Neuroimage*, vol. 6, no. 3, pp. 209–217, Oct. 1997, doi: 10.1006/nimg.1997.0290.
- [55] H. Jia, P.-T. Yap, and D. Shen, “Iterative multi-atlas-based multi-image segmentation with tree-based registration,” *Neuroimage*, vol. 59, no. 1, pp. 422–430, Jan. 2012, doi: 10.1016/j.neuroimage.2011.07.036.
- [56] G. Balakrishnan, A. Zhao, M. R. Sabuncu, J. Guttag, and A. V. Dalca, “VoxelMorph: A Learning Framework for Deformable Medical Image Registration,” *IEEE Trans. Med. Imaging*, vol. 38, no. 8, pp. 1788–1800, Aug. 2019, doi: 10.1109/TMI.2019.2897538.
- [57] S. Czolbe, P. Pegios, O. Krause, and A. Feragen, “Semantic similarity metrics for image registration,” *Medical Image Analysis*, vol. 87, p. 102830, Jul. 2023, doi: 10.1016/j.media.2023.102830.
- [58] M. Gross *et al.*, “Improved performance and consistency of deep learning 3D liver segmentation with heterogeneous cancer stages in magnetic resonance imaging,” *PLoS ONE*, vol. 16, no. 12, p. e0260630, Dec. 2021, doi: 10.1371/journal.pone.0260630.
- [59] B. Zhou, Z. Augenfeld, J. Chapiro, S. K. Zhou, C. Liu, and J. S. Duncan, “Anatomy-guided Multimodal Registration by Learning Segmentation without Ground Truth: Application to Intraoperative CBCT/MR Liver Segmentation and Registration.” arXiv, Apr. 14, 2021. Accessed: May 24, 2024. [Online]. Available: <http://arxiv.org/abs/2104.07056>

- [60] B. B. Avants, N. J. Tustison, J. Wu, P. A. Cook, and J. C. Gee, “An Open Source Multivariate Framework for n-Tissue Segmentation with Evaluation on Public Data,” *Neuroinform*, vol. 9, no. 4, pp. 381–400, Dec. 2011, doi: 10.1007/s12021-011-9109-y.
- [61] L. Zbinden *et al.*, “Convolutional neural network for automated segmentation of the liver and its vessels on non-contrast T1 vibe Dixon acquisitions,” *Sci Rep*, vol. 12, no. 1, p. 22059, Dec. 2022, doi: 10.1038/s41598-022-26328-2.
- [62] J. M. J. Valanarasu, V. A. Sindagi, I. Hacihaliloglu, and V. M. Patel, “KiU-Net: Overcomplete Convolutional Architectures for Biomedical Image and Volumetric Segmentation.” arXiv, Oct. 14, 2021. Accessed: May 24, 2024. [Online]. Available: <http://arxiv.org/abs/2010.01663>
- [63] A. Turečková, T. Tureček, Z. Komínková Oplatková, and A. Rodríguez-Sánchez, “Improving CT Image Tumor Segmentation Through Deep Supervision and Attentional Gates,” *Front. Robot. AI*, vol. 7, p. 106, Aug. 2020, doi: 10.3389/frobt.2020.00106.
- [64] K. Wang *et al.*, “Automated CT and MRI Liver Segmentation and Biometry Using a Generalized Convolutional Neural Network,” *Radiology: Artificial Intelligence*, vol. 1, no. 2, p. 180022, Mar. 2019, doi: 10.1148/ryai.2019180022.
- [65] P. F. Christ *et al.*, “Automatic Liver and Tumor Segmentation of CT and MRI Volumes using Cascaded Fully Convolutional Neural Networks.” arXiv, Feb. 23, 2017. Accessed: May 27, 2024. [Online]. Available: <http://arxiv.org/abs/1702.05970>
- [66] F. Isensee, P. F. Jaeger, S. A. A. Kohl, J. Petersen, and K. H. Maier-Hein, “nnU-Net: a self-configuring method for deep learning-based biomedical image segmentation,” *Nat Methods*, vol. 18, no. 2, pp. 203–211, Feb. 2021, doi: 10.1038/s41592-020-01008-z.
- [67] R. M. Haralick, K. Shanmugam, and I. Dinstein, “Textural Features for Image Classification,” *IEEE Trans. Syst., Man, Cybern.*, vol. SMC-3, no. 6, pp. 610–621, Nov. 1973, doi: 10.1109/TSMC.1973.4309314.
- [68] P. Prasanna, P. Tiwari, and A. Madabhushi, “Co-occurrence of Local Anisotropic Gradient Orientations (CoLIAGe): A new radiomics descriptor,” *Sci Rep*, vol. 6, no. 1, p. 37241, Nov. 2016, doi: 10.1038/srep37241.
- [69] B. Avants, C. Epstein, M. Grossman, and J. Gee, “Symmetric diffeomorphic image registration with cross-correlation: Evaluating automated labeling of elderly and neurodegenerative brain,” *Medical Image Analysis*, vol. 12, no. 1, pp. 26–41, Feb. 2008, doi: 10.1016/j.media.2007.06.004.
- [70] P. Bilic *et al.*, “The Liver Tumor Segmentation Benchmark (LiTS),” *Medical Image Analysis*, vol. 84, p. 102680, Feb. 2023, doi: 10.1016/j.media.2022.102680.
- [71] A. E. Kavur, “CHAOS Challenge - combined (CT-MR) healthy abdominal organ segmentation,” *Medical Image Analysis*, 2021.
- [72] A. Klein *et al.*, “Evaluation of 14 nonlinear deformation algorithms applied to human brain MRI registration,” *NeuroImage*, vol. 46, no. 3, pp. 786–802, Jul. 2009, doi: 10.1016/j.neuroimage.2008.12.037.

- [73] T. Heimann *et al.*, “Comparison and Evaluation of Methods for Liver Segmentation From CT Datasets,” *IEEE TRANSACTIONS ON MEDICAL IMAGING*, vol. 28, no. 8, 2009.
- [74] S. K. Zhou, D. Rueckert, and G. Fichtinger, Eds., *Handbook of Medical Image Computing and Computer Assisted Intervention*. Elsevier, 2020. Accessed: May 27, 2022. [Online]. Available: <https://linkinghub.elsevier.com/retrieve/pii/C20170046086>
- [75] K. Atesok, D. Galos, L. M. Jazrawi, and K. A. Egol, “Preoperative planning in orthopaedic surgery: current practice and evolving applications,” *Bulletin of the NYU Hospital for Joint Diseases*, vol. 73, no. 4, pp. 257–257, Oct. 2015.
- [76] D. M. Steinbacher, “Three-Dimensional Analysis and Surgical Planning in Craniomaxillofacial Surgery,” *Journal of Oral and Maxillofacial Surgery*, vol. 73, no. 12, pp. S40–S56, Dec. 2015, doi: 10.1016/j.joms.2015.04.038.
- [77] J. Nilsson, F. Nysjö, I. Nyström, J. Kämpe, and A. Thor, “Evaluation of in-house, haptic assisted surgical planning for virtual reduction of complex mandibular fractures,” *Int J CARS*, vol. 16, no. 6, pp. 1059–1068, Jun. 2021, doi: 10.1007/s11548-021-02353-w.
- [78] J. Wadley, N. Dorward, N. Kitchen, and D. Thomas, “Pre-operative planning and intra-operative guidance in modern neurosurgery: a review of 300 cases,” *Ann R Coll Surg Engl*, p. 9, 1999.
- [79] H. Algethami, F. C. Lam, R. Rojas, and E. M. Kasper, “Pre-Surgical and Surgical Planning in Neurosurgical Oncology - A Case-Based Approach to Maximal Safe Surgical Resection in Neurosurgery,” in *Frontiers in Clinical Neurosurgery*, X. Lv, G. Wang, J. Wang, and Z. Wu, Eds., IntechOpen, 2021. doi: 10.5772/intechopen.99155.
- [80] P. Jannin and X. Morandi, “Surgical models for computer-assisted neurosurgery,” *NeuroImage*, vol. 37, no. 3, pp. 783–791, Sep. 2007, doi: 10.1016/j.neuroimage.2007.05.034.
- [81] O. I. Craciunescu *et al.*, “Dynamic Contrast-Enhanced MRI in Head-and-Neck Cancer: The Impact of Region of Interest Selection on the Intra- and Interpatient Variability of Pharmacokinetic Parameters,” *International Journal of Radiation Oncology*Biophysics*, vol. 82, no. 3, pp. e345–e350, Mar. 2012, doi: 10.1016/j.ijrobp.2011.05.059.
- [82] S. Kobayashi, N. Saito, H. Horiuchi, R. Iorio, and K. Takaoka, “Poor bone quality or hip structure as risk factors affecting survival of total-hip arthroplasty,” *The Lancet*, vol. 355, no. 9214, pp. 1499–1504, Apr. 2000, doi: 10.1016/S0140-6736(00)02164-4.
- [83] A. S. Wong, A. M. R. New, G. Isaacs, and M. Taylor, “Effect of Bone Material Properties on the Initial Stability of a Cementless Hip Stem: A Finite Element Study,” *Proc Inst Mech Eng H*, vol. 219, no. 4, pp. 265–275, Apr. 2005, doi: 10.1243/095441105X34293.
- [84] R. Bryan, P. B. Nair, and M. Taylor, “Use of a statistical model of the whole femur in a large scale, multi-model study of femoral neck fracture risk,” *Journal of Biomechanics*, vol. 42, no. 13, pp. 2171–2176, Sep. 2009, doi: 10.1016/j.jbiomech.2009.05.038.

- [85] S. M. Goobie *et al.*, “Population Pharmacokinetics of Tranexamic Acid in Paediatric Patients Undergoing Craniostylosis Surgery,” *Clin Pharmacokinet*, vol. 52, no. 4, pp. 267–276, Apr. 2013, doi: 10.1007/s40262-013-0033-1.
- [86] J. Cates, S. Elhabian, and R. Whitaker, “Shapeworks: particle-based shape correspondence and visualization software.,” in *Statistical Shape and Deformation Analysis*, Elsevier, 2017, pp. 257–298. doi: 10.1016/B978-0-12-810493-4.00012-2.
- [87] A. Goparaju *et al.*, “On the Evaluation and Validation of Off-the-shelf Statistical Shape Modeling Tools: A Clinical Application,” *arXiv:1810.03987 [cs]*, Oct. 2018, Accessed: Apr. 06, 2022. [Online]. Available: <http://arxiv.org/abs/1810.03987>
- [88] F. Ambellan, H. Lamecker, C. von Tycowicz, and S. Zachow, “Statistical Shape Models: Understanding and Mastering Variation in Anatomy,” in *Biomedical Visualisation*, vol. 1156, P. M. Rea, Ed., in *Advances in Experimental Medicine and Biology*, vol. 1156. , Cham: Springer International Publishing, 2019, pp. 67–84. doi: 10.1007/978-3-030-19385-0_5.
- [89] T. Heimann and H.-P. Meinzer, “Statistical shape models for 3D medical image segmentation: A review,” *Medical Image Analysis*, vol. 13, no. 4, pp. 543–563, Aug. 2009, doi: 10.1016/j.media.2009.05.004.
- [90] V. Pekar, T. R. McNutt, and M. R. Kaus, “Automated model-based organ delineation for radiotherapy planning in prostatic region,” *International Journal of Radiation Oncology*Biophysics*Physics*, vol. 60, no. 3, pp. 973–980, Nov. 2004, doi: 10.1016/j.ijrobp.2004.06.004.
- [91] G. Zheng, S. Gollmer, S. Schumann, X. Dong, T. Feilkas, and M. A. González Ballester, “A 2D/3D correspondence building method for reconstruction of a patient-specific 3D bone surface model using point distribution models and calibrated X-ray images,” *Medical Image Analysis*, vol. 13, no. 6, pp. 883–899, Dec. 2009, doi: 10.1016/j.media.2008.12.003.
- [92] N. Rodriguez-Florez *et al.*, “Statistical shape modelling to aid surgical planning: associations between surgical parameters and head shapes following spring-assisted cranioplasty,” *Int J CARS*, vol. 12, no. 10, pp. 1739–1749, Oct. 2017, doi: 10.1007/s11548-017-1614-5.
- [93] B. Rigaud *et al.*, “Statistical Shape Model to Generate a Planning Library for Cervical Adaptive Radiotherapy,” *IEEE Trans. Med. Imaging*, vol. 38, no. 2, pp. 406–416, Feb. 2019, doi: 10.1109/TMI.2018.2865547.
- [94] I. Oguz *et al.*, “Entropy-based particle correspondence for shape populations,” *Int J CARS*, vol. 11, no. 7, pp. 1221–1232, Jul. 2016, doi: 10.1007/s11548-015-1319-6.
- [95] A. Goparaju *et al.*, “Benchmarking off-the-shelf statistical shape modeling tools in clinical applications.” *arXiv*, Sep. 06, 2020. Accessed: Jun. 15, 2022. [Online]. Available: <http://arxiv.org/abs/2009.02878>

- [96] Cootes T.F., Taylor C.J., Cooper D.H., Graham J., “Active shape models - their training and application.” [Online]. Available: *Computer Vision and Image Understanding*, 61 (1), pp. 38-59.
- [97] M. Lüthi *et al.*, “Statismo - A framework for PCA based statistical models,” *The Insight Journal*, Jul. 2012, doi: 10.54294/4eli51.
- [98] R. H. Davies, C. J. Twining, T. F. Cootes, J. C. Waterton, and C. J. Taylor, “3D Statistical Shape Models Using Direct Optimisation of Description Length,” in *Computer Vision — ECCV 2002*, vol. 2352, A. Heyden, G. Sparr, M. Nielsen, and P. Johansen, Eds., in *Lecture Notes in Computer Science*, vol. 2352., Berlin, Heidelberg: Springer Berlin Heidelberg, 2002, pp. 3–20. doi: 10.1007/3-540-47977-5_1.
- [99] S. Durrleman, X. Pennec, A. Trouvé, and N. Ayache, “Statistical models of sets of curves and surfaces based on currents,” *Medical Image Analysis*, vol. 13, no. 5, pp. 793–808, Oct. 2009, doi: 10.1016/j.media.2009.07.007.
- [100] J. L. Bruse *et al.*, “A statistical shape modelling framework to extract 3D shape biomarkers from medical imaging data: assessing arch morphology of repaired coarctation of the aorta,” *BMC Med Imaging*, vol. 16, no. 1, p. 40, Dec. 2016, doi: 10.1186/s12880-016-0142-z.
- [101] A. Kelemen, G. Szekely, and G. Gerig, “Elastic model-based segmentation of 3-D neuroradiological data sets,” *IEEE Trans. Med. Imaging*, vol. 18, no. 10, pp. 828–839, Oct. 1999, doi: 10.1109/42.811260.
- [102] M. Styner *et al.*, “Framework for the Statistical Shape Analysis of Brain Structures using SPHARM-PDM,” *The Insight Journal*, Jul. 2006, doi: 10.54294/owxzil.
- [103] M. Styner, “Boundary and medial shape analysis of the hippocampus in schizophrenia,” *Medical Image Analysis*, vol. 8, no. 3, pp. 197–203, Sep. 2004, doi: 10.1016/j.media.2004.06.004.
- [104] B. B. Avants *et al.*, “The optimal template effect in hippocampus studies of diseased populations,” *NeuroImage*, vol. 49, no. 3, pp. 2457–2466, Feb. 2010, doi: 10.1016/j.neuroimage.2009.09.062.
- [105] B. B. Avants, N. J. Tustison, G. Song, P. A. Cook, A. Klein, and J. C. Gee, “A reproducible evaluation of ANTs similarity metric performance in brain image registration,” *NeuroImage*, vol. 54, no. 3, pp. 2033–2044, Feb. 2011, doi: 10.1016/j.neuroimage.2010.09.025.
- [106] W. Bai *et al.*, “A bi-ventricular cardiac atlas built from 1000+ high resolution MR images of healthy subjects and an analysis of shape and motion,” *Medical Image Analysis*, vol. 26, no. 1, pp. 133–145, Dec. 2015, doi: 10.1016/j.media.2015.08.009.
- [107] J. Seidlitz *et al.*, “A population MRI brain template and analysis tools for the macaque,” *NeuroImage*, vol. 170, pp. 121–131, Apr. 2018, doi: 10.1016/j.neuroimage.2017.04.063.

- [108] M. Jenkinson, C. F. Beckmann, T. E. J. Behrens, M. W. Woolrich, and S. M. Smith, “FSL,” *NeuroImage*, vol. 62, no. 2, pp. 782–790, Aug. 2012, doi: 10.1016/j.neuroimage.2011.09.015.
- [109] Y. Ou, A. Sotiras, N. Paragios, and C. Davatzikos, “DRAMMS: Deformable registration via attribute matching and mutual-saliency weighting,” *Medical Image Analysis*, vol. 15, no. 4, pp. 622–639, Aug. 2011, doi: 10.1016/j.media.2010.07.002.
- [110] D. Vogel, A. Shah, J. Coste, J.-J. Lemaire, K. Wårdell, and S. Hemm, “Anatomical brain structures normalization for deep brain stimulation in movement disorders,” *NeuroImage: Clinical*, vol. 27, p. 102271, 2020, doi: 10.1016/j.nicl.2020.102271.
- [111] A. Updegrove, N. M. Wilson, and S. C. Shadden, “Boolean and smoothing of discrete polygonal surfaces,” *Advances in Engineering Software*, vol. 95, pp. 16–27, May 2016, doi: 10.1016/j.advengsoft.2016.01.015.
- [112] D. L. G. Hill, P. G. Batchelor, M. Holden, and D. J. Hawkes, “Medical image registration,” p. 46.
- [113] F. Alam, S. U. Rahman, S. Ullah, and K. Gulati, “Medical image registration in image guided surgery: Issues, challenges and research opportunities,” *Biocybernetics and Biomedical Engineering*, vol. 38, no. 1, pp. 71–89, 2018, doi: 10.1016/j.bbe.2017.10.001.
- [114] J. M. Fitzpatrick, “The role of registration in accurate surgical guidance,” *Proc Inst Mech Eng H*, vol. 224, no. 5, pp. 607–622, May 2010, doi: 10.1243/09544119JEIM589.
- [115] H. Liu and F. R. Y. Baena, “Automatic Markerless Registration and Tracking of the Bone for Computer-Assisted Orthopaedic Surgery,” *IEEE Access*, vol. 8, pp. 42010–42020, 2020, doi: 10.1109/ACCESS.2020.2977072.
- [116] C. Gao *et al.*, “Fiducial-Free 2D/3D Registration for Robot-Assisted Femoroplasty,” *IEEE Trans. Med. Robot. Bionics*, vol. 2, no. 3, pp. 437–446, Aug. 2020, doi: 10.1109/TMRB.2020.3012460.
- [117] N. Loy Rodas, M. Decrouez, B. Bleunven, and S. Cahen, “In-vivo bone segmentation approach for Total Knee Arthroplasty,” presented at the CAOS 2020. The 20th Annual Meeting of the International Society for Computer Assisted Orthopaedic Surgery, pp. 183–177. doi: 10.29007/d78d.
- [118] J.-D. Lee, C.-H. Huang, T.-C. Huang, H.-Y. Hsieh, and S.-T. Lee, “Medical augment reality using a markerless registration framework,” *Expert Systems with Applications*, vol. 39, no. 5, pp. 5286–5294, Apr. 2012, doi: 10.1016/j.eswa.2011.11.009.
- [119] H. Suenaga *et al.*, “Vision-based markerless registration using stereo vision and an augmented reality surgical navigation system: a pilot study,” *BMC Med Imaging*, vol. 15, no. 1, p. 51, Dec. 2015, doi: 10.1186/s12880-015-0089-5.
- [120] M. Yin, X. Shen, Y. Hu, and X. Fang, “An Automatic Registration Method Based on Fiducial Marker for Image Guided Neurosurgery System,” in *AsiaSim 2013*, vol. 402, G. Tan, G. K. Yeo, S. J. Turner, and Y. M. Teo, Eds., in Communications in Computer and

Information Science, vol. 402. , Berlin, Heidelberg: Springer Berlin Heidelberg, 2013, pp. 114–125. doi: 10.1007/978-3-642-45037-2_11.

- [121] S. Sta, J. Ogor, H. Letissier, E. Stindel, C. Hamitouche, and G. Dardenne, “Towards markerless computer assisted surgery: Application to total knee arthroplasty,” *Int J Med Robot*, vol. 17, no. 5, Oct. 2021, doi: 10.1002/rcs.2296.
- [122] I. M. Germano, Ed., *Advanced techniques in image-guided brain and spine surgery*. New York: Thieme, 2002.
- [123] S. Kim and P. Kazanzides, “Fiducial-based registration with a touchable region model,” *Int J CARS*, vol. 12, no. 2, pp. 277–289, Feb. 2017, doi: 10.1007/s11548-016-1477-1.
- [124] Q.-Y. Zhou, J. Park, and V. Koltun, “Open3D: A Modern Library for 3D Data Processing,” *arXiv:1801.09847 [cs]*, Jan. 2018, Accessed: Aug. 10, 2021. [Online]. Available: <http://arxiv.org/abs/1801.09847>
- [125] Y. Zhong, “Intrinsic shape signatures: A shape descriptor for 3D object recognition,” in *2009 IEEE 12th International Conference on Computer Vision Workshops, ICCV Workshops*, Kyoto, Japan: IEEE, Sep. 2009, pp. 689–696. doi: 10.1109/ICCVW.2009.5457637.
- [126] F. Tombari, S. Salti, and L. Di Stefano, “Performance Evaluation of 3D Keypoint Detectors,” *Int J Comput Vis*, vol. 102, no. 1–3, pp. 198–220, Mar. 2013, doi: 10.1007/s11263-012-0545-4.
- [127] X. Fan, D. W. Roberts, S. Ji, A. Hartov, and K. D. Paulsen, “Intraoperative fiducial-less patient registration using volumetric 3D ultrasound: a prospective series of 32 neurosurgical cases,” *JNS*, vol. 123, no. 3, pp. 721–731, Sep. 2015, doi: 10.3171/2014.12.JNS141321.